Graphene FET Sensors for Alzheimer's Disease Protein Biomarker Clusterin Detection

Theodore Bungon[1], Carrie J. Haslam[1], Samar Damiati[2], Benjamin O'driscoll[1], Toby Whitley[1], Paul Davey[1], Giuliano Siligardi[3], Jerome Charmet[4], Shakil A. Awan[1*]

[1]University of Plymouth, United Kingdom, [2]King Abdulaziz University, Saudi Arabia, [3]Diamond Light Source (United Kingdom), United Kingdom, [4]University of Warwick, United Kingdom

Submitted to Journal:
Frontiers in Molecular Biosciences

Specialty Section:
Molecular Diagnostics and Therapeutics

Article type:
Original Research Article

Manuscript ID:
651232

Received on:
08 Jan 2021

Revised on:
28 Feb 2021

Journal website link:
www.frontiersin.org

Conflict of interest statement

The authors declare that the research was conducted in the absence of any commercial or financial relationships that could be construed as a potential conflict of interest

Author contribution statement

Conceptualization, S.A.A.; methodology, S.A.A., T.B., C.H., S.D. and B.O.; software, B.O. and T.B.; validation, S.A.A., T.B., G.S., and J.C.; formal analysis, S.A.A.; data curation, S.A.A.; writing—original draft preparation, S.A.A and T.B.; writing—review and editing, All; supervision, S.A.A.; T.W., and P.D.; project administration, S.A.A; funding acquisition, S.A.A. All authors have read and agreed to the published version of the manuscript.

Keywords

Graphene, Field-effect transistors, Biosensors, Clusterin Protein, Alzheimer's disease, SRCD Absorbance Spectroscopy

Abstract

Word count: 262

We report on the fabrication and characterisation of graphene field-effect transistor (GFET) biosensors for the detection of Clusterin, a prominent protein biomarker of Alzheimer's disease (AD). The GFET sensors were fabricated on Si/SiO2 substrate using photolithographic patterning and metal lift-off techniques with evaporated chromium and sputtered gold contacts. Raman Spectroscopy was performed on the devices to determine the quality of the graphene. The GFETs were annealed to improve their performance before the channels were functionalized by immobilising the graphene surface with linker molecules and anti-Clusterin antibodies. Concentration of linker molecules was also independently verified by absorption spectroscopy using the highly collimated micro-beam light of Diamond B23 beamline. The detection was achieved through the binding reaction between the antibody and varying concentrations of Clusterin antigen from 1 pg/mL to 100 pg/mL, as well as specificity tests using human chorionic gonadotropin (hCG), a glycoprotein risk biomarker of certain cancers. The GFETs were characterized using direct current (DC) 4-probe electrical resistance (4-PER) measurements, which demonstrated a limit of detection of the biosensors to be ~ 300 fg/mL (4 fM). Comparions with back-gated Dirac voltage shifts with varying concentration of Clusterin show 4-PER measurements to be more accurate, at present, and point to a requirement for further optimisation of the fabrication processes for our next generation of GFET sensors. Thus, we have successfully fabricated a promising set of GFET biosensors for the detection of Clusterin protein biomarker. The developed GFET biosensors are entirely generic and also have the potential to be applied to a variety of other disease detection applications such as Parkinson's, cancer and cardiovascular.

Contribution to the field

This study describes novel graphene field-effect transistor (GFET) sensors for detecting Clusterin protein biomarker, a prominent biomarker of Alzheimer's Disease (AD). We detail the fabrication of the sensors, their bio-functionalisation and detection using a 4-probe direct current electrical resistance measurement approach. This approach is distinct from the traditional 3-probe electrochemical approach and is found to be highly repeatable and sensitive. Here, we have demonstrated ultra-high sensitive detection of Clusterin from 1pg/mL to 100 pg/mL concentration range with a limit-of-detection of 210 fg/mL. In addition, we also demonstrate that the GFET sensors are highly specific as they showed negligible response to hCG protein (biomarker of certain cancers) when a concentration of 100 ng/mL concentration was drop-cast onto the sensors (which is a factor of x1000 higher than the 100 pg/mL Clusterin). Thus, our GFET sensors show five times higher sensitivity (210 fg/mL vs 1pg/mL limit-of-detection listed in Table 3) than comparable sensors (and detection methods) reported in the literature and open exciting opportunities for point-of-care, low cost and accurate applications of our sensors in the near future.

Funding statement

This research was funded by University of Plymouth (C.H.: GD105227-104, B.O'D.: GD110025-104), Diamond Light Source, DLS-SM24459-1 and EPSRC under contract number EP/M006301/1.

Ethics statements

Studies involving animal subjects
Generated Statement: No animal studies are presented in this manuscript.

Studies involving human subjects
Generated Statement: No human studies are presented in this manuscript.

Inclusion of identifiable human data
Generated Statement: No potentially identifiable human images or data is presented in this study.

Data availability statement

Generated Statement: The original contributions presented in the study are included in the article/supplementary material, further inquiries can be directed to the corresponding author/s.

Graphene FET Sensors for Alzheimer's Disease Protein Biomarker Clusterin Detection

Theodore Bungon[1], Carrie Haslam[1], Samar Damiati[2,3], Benjamin O'Driscoll[1], Toby Whitley[1], Paul Davey[1], Giuliano Siligardi[4] and Jerome Charmet[5], Shakil A. Awan[1*]

[1] Wolfson Nanomaterials and Devices Laboratory, School of Engineering, Computing and Mathematics, Faculty of Science and Engineering, University of Plymouth, Drake Circus, Plymouth, Devon, United Kingdom

[2] Department of Biochemistry, Faculty of Science, King Abdulaziz University (KAU), Jeddah, Saudi Arabia

[3] Division of Nanobiotechnology, Department of Protein Science, Science for Life Laboratory, School of Engineering Sciences in Chemistry, Biotechnology and Health, KTH Royal institute of Technology, Stockholm, Sweden

[4] Diamond Light Source, Rutherford Appleton Laboratory, Oxfordshire, United Kingdom

[5] Institute of Digital Healthcare, WMG, University of Warwick, Coventry, United Kingdom

*** Correspondence:**
Shakil Awan
shakil.awan@plymouth.ac.uk

Keywords: graphene[1], FET[2], biosensor[3], 4-probe electrical detection[4], Clusterin[5], Alzheimer's disease[6], protein biomarkers[7], absorbance spectroscopy[8].

Abstract

We report on the fabrication and characterisation of graphene field-effect transistor (GFET) biosensors for the detection of Clusterin, a prominent protein biomarker of Alzheimer's disease (AD). The GFET sensors were fabricated on Si/SiO_2 substrate using photolithographic patterning and metal lift-off techniques with evaporated chromium and sputtered gold contacts. Raman Spectroscopy was performed on the devices to determine the quality of the graphene. The GFETs were annealed to improve their performance before the channels were functionalized by immobilising the graphene surface with linker molecules and anti-Clusterin antibodies. Concentration of linker molecules was also independently verified by absorption spectroscopy using the highly collimated micro-beam light of Diamond B23 beamline. The detection was achieved through the binding reaction between the antibody and varying concentrations of Clusterin antigen from 1 pg/mL to 100 pg/mL, as well as specificity tests using human chorionic gonadotropin (hCG), a glycoprotein risk biomarker of certain cancers. The GFETs were characterized using direct current (DC) 4-probe electrical resistance (4-PER) measurements, which demonstrated a limit of detection of the biosensors to be ~ 300 fg/mL (4 fM). Comparions with back-gated Dirac voltage shifts with varying concentration of Clusterin show 4-PER measurements to be more accurate, at present, and point to a requirement for further optimisation of the fabrication processes for our next generation of GFET sensors. Thus, we have successfully fabricated a promising set of GFET biosensors for the detection of Clusterin protein biomarker. The developed GFET biosensors are entirely generic and also have the potential to be applied to a variety of other disease detection applications such as Parkinson's, cancer and cardiovascular.

1 Introduction

Graphene, a single atomic plane of carbon, was considered to be thermodynamically unstable until 17 years ago. In 2004, Novoselov et al. (Novoselov, Geim et al. 2004) experimentally demonstrated that graphene can exist in the free state at room temperature, and that it is stable as a single layer of graphene making it a zero bandgap semiconductor. The monolayer of sp^2 bonded carbon atoms is tightly packed into a two-dimensional (2D) sheet arranged in a honeycomb lattice. Graphene has the potential to advance many technological areas because of its outstanding material properties such as its high carrier mobility (Novoselov, Geim et al. 2004, Novoselov, Jiang et al. 2005, Bolotin, Sikes et al. 2008, Morozov, Novoselov et al. 2008), current carrying capacity (Castro Neto, Guinea et al. 2009), thermal conductivity (Balandin, Ghosh et al. 2008), optical properties (Blake, Brimicombe et al. 2008) and mechanical stability (Booth, Blake et al. 2008). It is being researched for various applications such as high-speed electronics (Lin, Dimitrakopoulos et al. 2010, Awan, Lombardo et al. 2016), optoelectronics (Bao and Loh 2012), solar cells (Wang, Zhi et al. 2008), energy storage (Wang, Shi et al. 2009), electromechanical resonators (Bunch, van der Zande et al. 2007), composites (Stankovich, Dikin et al. 2006) and biosensors (Justino, Gomes et al. 2017, Haslam, Damiati et al. 2018, Vu and Chen 2019).

Graphene is ideally suited to applications in biosensing due to its large surface-to-volume ratio, biocompatibility, chemical stability, ease of surface functionalisation, field effect-based ambipolar transport of electrons and holes and excellent electrical conductivity (Geim and Novoselov 2010), which are highly beneficial for good sensor performance such as increased sensitivity and a low limit of detection (LOD). Among the many graphene-based biosensor applications, graphene field-effect transistors (GFETs) are widely regarded as a promising platform for biosensing (Haslam, Damiati et al. 2018, Bungon, Haslam et al. 2020). The graphene channel in GFETs is typically exposed to the charged biological environment and is able to detect the presence of biomolecules electrically, based on resistance/conductance change caused by the binding of receptor molecules with a given antigen biomarker (enzymes, proteins, peptides, DNA, etc). (Dong, Shi et al. 2010, Okamoto, Ohno et al. 2012, Vu and Chen 2019). GFET is a powerful biosensing platform due to its relative simplicity in sensor preparation but also high signal-to-noise ratio, low-cost, portability and relative eas of integration with a range of existing electronic systems. GFETs consume less energy, can be scaled down and can operate at higher frequencies making them a flexible platform for biosensing (Novoselov, Geim et al. 2004, Novoselov, Geim et al. 2005, Awan, Lombardo 2016). Such GFET biosensors are being researched extensively for early diagnosis of not only Alzheimer's disease but also for a variety of other diseases such as Parkinson's, cancer and cardiovascular.

Here, we report on the detection of Clusterin, a prominent protein biomarker of Alzheimer's disease (AD) using both electrical and B23 absorption spectroscopy approaches. AD is a sub-type of dementia responsible for around 60-70% of cases in neurodegenerative diseases. There are approximately 54 million people currently living with dementia worldwide and this number is expected to rise to 130 million by 2050, and an estimated 9.9 million people will develop the disease every year (Alzheimer's Society 2020). AD is an incurable and long-term neurodegenerative disease that progressively worsens over time. It is believed to be caused by abnormal build-up of proteins in and around the brain. Tests have revealed deposits of protein around the extracellular and intracellular compartments of a post-mortem AD brain, the intracellular deposits were made up of filaments of hyperphosphorylated tau protein (Iqbal, Alonso Adel et al. 2005). Evidence has shown that neurofibrillary tangles (NFTs), consisting of hyperphosphorylated tau, are present within the neurons of AD patients; NFTs disrupt the normal communication between neurons (Selkoe 1991). While the extracellular deposits also known as

amyloid plagues are most commonly found in the neocortex (responsible for sensory perception, reasoning, conscious thoughts, generation of motor commands and language in humans). The neocortex consists of 4-kDa polypeptide known as the β-amyloid (Aβ) (Glenner and Wong 1984, Masters, Simm et al. 1985). Research has shown considerable evidence that neurodegeneration that occurs in AD patients is as a result of the accumulation and aggregation of Aβ. Aβ plaques are formed within the medial temporal lobe and also within the cerebral cortex of the brain tissue. This Aβ formation is attributed to the abnormal metabolism of β-amyloid precursor protein (APP) (Hardy and Selkoe 2002). The Aβ plaques and NFTs develop over a long period of time (~20-30 years) and leads to death of nerve cells and loss of brain tissues. Clusterin (is encoded by the single copy CLU gene located at the p21 – p12 locus on chromosome 8 in humans), also known as apolipoprotein-J, is a glycoprotein found in various tissues and bodily fluids (De Silva, Stuart et al. 1990), and it functions as an extracellular chaperone (Satapathy 2017). Increased levels of Clusterin have been found in the frontal cortex and hippocampus of post-mortem AD brain tissue (May, Lampert-Etchells et al. 1990, Lidström, Bogdanovic et al. 1998). It was demonstrated that CLU is strongly associated to soluble Aβ in the cerebral spinal fluid (CSF) (Ghiso, Matsubara et al. 1993), and it can either prevent the aggregation of Aβ or increase its solubility (Matsubara, Soto et al. 1996). It regulates the formation and toxicity of Aβ fibril, and also aids in transporting Aβ across the blood–brain barrier. Clusterin has a molecular weight of 75-80 kDa and is comprised of 449 amino acids (Tsuruta, Wong et al. 1990, James, Hochstrasser et al. 1991), two ~40 kDa subunits of α and β connected by five disulphide bond motif (Kirszbaum, Bozas et al. 1992). Clusterin plays an important role in the progression of AD and it has been identified as one of the key biomarkers of AD (Thambisetty, Simmons et al. 2010). It was experimentally shown that Clusterin was elevated by ~40% above non-demented controls in the brain of AD patients (May, Lampert-Etchells et al. 1990, Oda, Pasinetti et al. 1994). Different Clusterin levels have been reported for AD patients;, 67 AD cases were studied with mean age 85.3 ± 3.2 and Clusterin plasma levels of 158.5 ± 45.3 µg/mL (Schürmann, Wiese et al. 2011), 60 AD cases were studied with mean age 83.4 ± 7.3 with Clusterin plasma levels of 129 ± 29 µg/mL (Schrijvers, Koudstaal et al. 2011), also 17 AD cases with mean age 86.0 ± 6.36 and Clusterin plasma levels of 106.3 ± 23.7 µg/mL (Thambisetty, An et al. 2012). Currently, diagnosis of AD can take up to two years involving a range of different tests such as computer tomography (CT), magnetic resonance imaging (MRI),Positron emission tomography (PET), neurological evaluation, cognitive and neuropsychological tests (Clinic 2020). Therefore, the need for a fast, low-cost, accurate, non-invasive, and portable means of diagnosing Alzheimer's disease at an early stage is of high importance. Here we demonstrate the sensitivty, repeatability and specificity of the GFET biosensors for the detection of pure proteins. The next stage of the study will be to investigate the sensor response using real patient samples (such as serum, plasma or blood), stability and storage of the sensors (Zupančič, Jolly et al. 2021, Leva-Bueno, Peyman et al. 2020, Teixeira, Burwell et al. 2014). Thus, GFET biosensors offer a unique route towards the development of vitally needed diagnostic platform for AD.

2 Materials and Methods

2.1 Materials

Monolayer graphene was produced by chemical vapour deposition (CVD) method on a 300 nm Si/SiO_2 substrate, supplied by Graphenea (San Sebastián, Spain) and LG Electronics Inc. (Gangseo-gu, Seoul, Korea). The chemicals used for the GFET fabrication were photoresist, lift-off resist (LoR), Microposit developer and Microposit remover, purchased from A-Gas Electronic Materials (Warwickshire, UK).

Recombinant human Clusterin protein and anti-Clusterin antibody were purchased from Abcam (Cambridge, UK). Linker molecule 1-pyrenebutanoic acid succinimidyl ester (Pyr-NHS),

bovine serum albumin (BSA) blocking solution and Phosphate-Buffered Saline (PBS) were purchased from Sigma Aldrich (Dorset, UK). All measurements were performed at room temperature, pH of 7.4 and using 10 µL samples deposited on the GFET sensors.

The quality of graphene was evaluated using an XPLORA Raman spectroscopy system (HORIBA, Northampton, UK). All measurements on the XPLORA system were performed at a wavelength of 532 nm, with ~ 4 mW of incident power and a grating of 1200T. The XPLORA Raman system was interfaced with an OLYMPUS BX41 microscope (Shinjuku, Japan).

The electrical characterisation of the GFETs was performed under ambient conditions using a Keysight B1500A semiconductor device parameter analyser interfaced to a MPS150 probe station (Cascade Microtech, Thiendorf, Germany). The 4-probe current–voltage measurements (I_D–V_D and I_D–V_G) were acquired as a function of gate voltage (V_G) from −100 V to +100 V with I_D–V_D curves from −50 mV to +50 mV with a 100µA compliance. The I_D–V_D output and I_D–V_G transfer curves were measured at each functionalisation stage.

All absorption spectroscopy experiments were performed on Beamline B23 at Diamond Light Source (Oxfordshire, UK) over the 180 – 400 nm wavelength range, using a wavelength increment of 1nm, with cell path length of 1mm and at room temperature ~ 22 °C (Hussain, Jávorfi et al. 2012).

2.2 Fabrication of the Graphene FETs

The GFET sensors were fabricated on a p++ Si/SiO_2 substrate through the processes of photolithographic patterning and metal lift-off techniques with evaporated chromium and sputtered gold contacts. There are two major stages in the fabrication process, the first stage involves forming the graphene channel whereas the second stage involves forming the source, drain and voltage electrodes. A representation of the fabrication process is shown in **Figure 1**.

The formation of the graphene channels on the Si/SiO_2 substrate involves dicing the samples into sizes of 1cm x 1cm chips before spin-coating the samples with lift-off resist (LoR) at 3000 revolutions-per-minute (rpm) for 30 s. The samples are then pre-baked in a fan oven at 175 °C for 15 min. Pre-baking the samples solidify the LoR as it eases in lifting off the photoresist (PR) while protecting the graphene channels formed. The next step is spin-coating the samples with a layer of positive photoresist (PR) at 3000 rpm for 30 s and then post-baking on a hotplate at 100 °C for 60 s. The post-bake step is to solidify the PR and remove any solvents on the samples. The samples are then positioned in a mask-aligner under a patterned mask for creating the graphene channels, and exposed to ultra-violet (UV) radiation for 25 s. The samples are then rinsed in a chemical developer mixed with di-ionized water (20 mL developer mixed with 30mL di-ionized water), until the graphene channels are visible under a microscope. There is always residue of PR/PMMA (poly-methyl methacrylate) on the sample at this stage, which degrades the quality of the graphene, which can be reduced by post-baking the samples on a hotplate at 180 °C for 8 min under deep ultraviolet (DUV) light of 254 nm. The DUV dissociates the bonds between PR/PMMA and graphene and reduces contact resistance of the sample.

Next, the samples are transferred into a sputtering machine for Ar plasma etching. The unprotected graphene samples (not protected by PR) are then etched by plasma formed from the ionization of Ar gas particles in a vacuum of 6×10^{-7} Torr at 50W RF power for 2.5 min before the samples are treated with a chemical remover. Subsequently, the samples were placed in a chemical remover in an ultrasonic bath for ~1 h at 60 °C, the ultrasonic bath was turned off and the samples were left in the chemical remover for 15 h. The samples were then rinsed in di-ionised water and left to dry in a vacuum chamber for an hour.

The second fabrication stage involves forming metallic Cr and Au electrodes as the source, drain and voltage electrodes. The electrode formation follows the same process as the graphene channel formation, but the samples are post-baked in an oven at 120 °C for 15 min instead of exposing to DUV on a hotplate. Next, Cr is thermally evaporated using an Edwards Thermal

Evaporator. The Cr target was heated to ~2000 °C for 8 s in a vacuum pressure of 10^{-6} Torr to form a 5 nm layer of Cr on the graphene samples. Thermal evaporation is a gentle way of depositing Cr on the samples without destroying the graphene channels already formed, and the Cr layer functions as an adhesive layer between graphene and the Au metallic contacts (Haslam, Damiati et al. 2018). Using the Nordiko sputtering machine, 30 nm of Au was sputtered directly onto the Cr layer. The treatment with chemical remover was repeated and the samples were dried in a vacuum chamber for a further one hour.

The fabricated 1cm x 1cm chips consists of 15 GFET devices, 5 asymmetric GFETs with the graphene channel length of 720 µm and 10 symmetric GFETs with graphene channel length of 400 µm with both being 80 µm (Haslam, Damiati et al. 2018). Overall, the GFET sensors take approximately 3 days to fabricate and a further 1-2 days for biofunctionalisation and characterisation of the sensors. **Figure 2** shows two symmetric GFET sensors in series in a device (deployed in this study) and when they are exposed to Clusterin at a concentration of 1 pg/mL.

2.3 Functionalisation of GFETs

The GFETs were functionalised by immobilising the graphene surface with an anti-Clusterin antibody using a linker molecule, after which bovine serum albumin (BSA) was deposited and the final step involved conjugation of the Clusterin antigen in varying concentrations following the same protocol as Haslam, C. et al. (Haslam, Damiati et al. 2018). The steps involved in the biofunctionalisation processes are illustrated in **Figure 3**.

The Pyr-NHS ester linker molecules are a cross-linking agent that react with special functionalised groups such as amino groups on proteins. The linker molecule (1-pyrenebutanoic acid succinimidyl ester) used belongs to N-Hydroxysuccinimide (NHS) group known as Pyr-NHS ester. It has an aromatic pyrenyl group that strongly interacts with the surface of graphene via non-covalent π-π interactions and the succinimidyl ester group covalently reacts with the amino group (NH_2) of the antibody (Huang, Dong et al. 2011). The linker molecule was applied at a concentration of 2mM and was allowed to incubate at 4 °C for 4 h, after which it was rinsed thrice with PBS and allowed to dry in ambient temperature. Once dry, Raman and electrical characterisation were performed followed by the binding of anti-Clusterin antibody. The antibody (Ab) was applied at a concentration of 20 µg/mL and was allowed to incubate following the same procedure as for the linker stage. BSA was then deposited on the GFET to block sites between the Ab regions preventing non-specific binding. BSA increases the tendency of the antibody to bind with the antigen of interest and it also improves the sensitivity of the sensor by decreasing background noise as the additional sites are blocked (Biocompare 2012). BSA was deposited at a concentration of 0.5% and allowed to incubate following the same procedure as for the linker and Ab stages.

The final step involved depositing Clusterin antigen on the samples at varying concentrations from 1 pg/mL–100 pg/mL, followed by the samples being incubated for 1h at 37 °C before they were allowed to dry in ambient temperature and characterised using Raman spectroscopy and electrical 4-probe measurements (Awan, Kibble et al. March, 2011) .

3 Results

3.1 Characterization of GFETs

The GFETs were characterised using Raman Spectroscopy to analyse the quality of the graphene channels (Ferrari, Meyer et al. 2006) and also with a semiconductor device parameter analyser to determine the electrical properties of the GFETs. Raman Spectroscopy is one of the

most accurate, effective and non-destructive tool for the characterisation of graphene because of its sensitivity to important features and properties of graphene such as defect (Ferrari 2007), doping (Casiraghi, Pisana et al. 2007), strain (Huang, Yan et al. 2009) and temperature (Calizo, Balandin et al. 2007). The Raman spectrum of graphene is made up of three main features with different physical origins; they are the 2D peak previously known as G' peak, the G peak and D peak. In monolayer graphene, the 2D peak is observed at a Raman shift of ~2700 cm^{-1}, the G peak at a Raman shift of ~1580 cm^{-1} and the D peak at a Raman shift ~1350 cm^{-1} (Graf, Molitor et al. 2007, Mafra, Samsonidze et al. 2007). **Figure 4** shows Raman spectra of three devices after fabrication, the intensity ratio I(2D)/I(G) position for Ch-1T = ~ 1.10, Ch-1B = ~1.04 and Ch-2B = ~ 1.20 and full width half maximum (FWHM) of the 2D peak for Ch-1T = 59.8 cm^{-1}, Ch-1B = 66.9 cm^{-1} and Ch-2B = 54.9 cm^{-1}, which confirms the graphene channels are monolayer, and the D peak confirms the presence of defects, which is generally caused by the fabrication process.

The GFETs were electrically characterised using a Keysight B1500A semiconductor device parameter analyser interfaced to a Cascade probe station in ambient temperature and a four-probe I_D–V_D and I_D–V_G measurements were taken to study the electrical properties and performance of the sensors such as its sheet resistance, contact resistance, Dirac curve and mobility. I_D–V_D measurements were taken on each sensor with a voltage sweep from −50 mV to +50 V and compliance of 100 μA. The sensors showed a linear response in current from changes in drain voltage, showing the channels are Ohmic as shown in the inset of **Figure 5**. Back-gated measurements were also performed to obtain the I_D–V_G curve with a forward and reverse voltage sweep from -100 V to +100 V, with a fixed drain voltage of 50 mV, **Figure 5** (main panel). Data analysis was performed using the SCRAMBLE software which was developed in-house and graphs were plotted in Originlab. The I_D–V_G curves show the Dirac curve of the graphene channels, revealing that the three channels are hole doped. From the curves, the carrier mobility of the three channels is found to be around 500–600 cm^2/Vs (Zhong, Zhang et al. 2015, Bøggild, Mackenzie et al. 2017). **Table 1** shows the Dirac point voltages (forward and reverse) and resistances for all three channels.

During the transfer of CVD graphene onto a substrate, a polymer PMMA is used to support the graphene while the Cu substrate is etched. The PMMA often leaves a layer of residue on the graphene surface and the residue remains on the surface even after fabrication. The standard process of removing PMMA using acetone does not completely remove the residues because of strong Van der Waals interaction with graphene (Cheng, Zhou et al. 2011). The presence of the residue and also water molecules from the graphene surface degrade the transport properties of graphene, causing a weak p-doping (Lin, Lu et al. 2012). We explored the effect of annealing to remove these contaminants from the surface of graphene, thermally annealing GFETs improve their performance increasing carrier mobility of the graphene channels (Cheng, Zhou et al. 2011, Pirkle, Chan et al. 2011, Kumar, Kim et al. 2013). We annealed the GFET at 215 °C for 30 min. **Figure 4** shows results for Channel-1B at bare stage and after annealing. **Figure 6** shows results for Channel-1B at bare stage and after annealing.

After annealing, the resistance of the device decreased by 31% from ~4086 Ω to ~2822 Ω, and the carrier mobility increased by ~43% from 460 cm^2/Vs to 660 cm^2/Vs, improving the performance of the sensor. The annealed GFETs were then exposed to Pyr-NHS ester linker molecules using the drop-cast method, as shown in **Figure 2B** where the diameter of the solution drop is typically ~ 1mm. The linker molecules were also characterised using absorbance spectra, which could easily resolve a concentration level of 0.2 μg/mL, as shown in **Figure 7**. The data show clear triple peaks in absorbance due to the pyrene moiety that is central to the Pyr-NHS ester linker molecules, also observed by Baek et al. (Baek, Jung et al. 2011) after functionalising carbon nanotubes for electrical detection of DNA hybridisation. The data in **Figure 7** also show a repeat measurement (off-set for clarity) of the absorbance spectra over the 220–400 nm wavelength range, demonstrating excellent repeatability of the measurements. The independent absorbance spectra essentially served to increase our confidence in the linker solutions we deployed for the GFET sensor experiments.

Following the functionalisation of the GFETs, **Figures 8–10** show data from Channel-1B, Channel-1T and Channel-2B for I_D-V_D and I_D-V_G characteristic curves. **Figure 8A and 8B** shows data for bare to BSA functionalisation stages, with I_D–V_D showing linear Ohmic response and I_D-V_G showing shifts in the Dirac point from bare to linker stages. However, it is interesting to note the Dirac points are at approximately 100 V limit of our measurement system for antibody to BSA stages. Although the I_D-V_G characteristic curves provide quantitative indication of the influence of charged molecules on the surface of graphene, albeit with a relatively high standard deviation, at present a more robust quantitative response of the GFET sensors can be determined from the 4-PER measurements of the I_D-V_D curves. In contrast, **Figure 8C** shows the standard ohmic response for functionalisation stages from BSA to Clusterin (at 1 to 100 pg/mL concentration levels) and 100 ng/mL of human chorionic gonadotropin (hCG), whereas **Figure 8D** shows the Dirac point is approximately constant around 25 V. This is in agreement with our previous observations (Haslam, Damiati et al. 2018) that the Dirac point shift is typically in the few-volt region for similar concentrations of hCG and is significantly influenced by hysteresis and charge traps in the SiO_2 substrate. **Figures 9 and 10** show almost identical response of the GFETs from bare to Clusterin antigen and hCG antigen detection. **Table 2** shows the corresponding data from the GFET sensors from bare to Clusterin and hCG antigen stages based on the I_D-V_D results.

4. Discussion

Figure 11 shows plot of resistance change (Mean ± SD) for each channel at all stages of the functionalisation process. The data show that there is an approximate 30% reduction in resistance, from bare stage when the channels are annealed (inset in **Figure 11**). A further 30% reduction in resistance is observed when the linker molecules are bound to the graphene surface. In contrast, there is almost a negligible change in resistance when the antibodies and BSA interface with the linker functionalized GFETs. However, when 1pg/mL of Clusterin is conjugated with the antibodies on the GFETs, we observe an ~118% increase in resistance. We estimate a LoD ~300 fg/mL (4 fM) for Clusterin detection, similar to the LoD demonstrated for hCG detection by Haslam et al. (Haslam, Damiati et al. 2018) using our DC 4-PER measurement technique. The LoD was estimated using LoD ~ 3.3(σ/S), where σ is the standard deviation at low concentration (in our case at the BSA stage) and S is the sensitivity coefficient or slope of the calibration curve (over the log-linear dynamic range) shown in Fig. 11. The log-linear least squares solid line fit to the data shown in **Fig. 11** is effectively a partial fit of the Hill-Langmuir equation (Hill 1910, Langmuir 1918). **Figure 11** also shows a corresponding comparison with back-gated measurements of Dirac voltage shifts normalized with respect to the BSA stage. At 1pg/mL of Clusterin concentration the Dirac voltage shift of approximately 60 ± 22.9 V, from the BSA stage, is clearly discernable ($p < 0.001$). At subsequent concentrations of Clusterin, 10pg/mL and 100pg/mL, a clear reduction in the Dirac voltage shifts are observed. However, the standard deviations of the measurements are relatively large, as also observed by (Tsang, Lieberthal et al. 2019), and point to a future requirement for further optimisation of our next generation of GFETs and their fabrication processes. The initial 60 ± 22.9 V increase in Dirac voltage shift at 1pg/mL Clusterin concentration and the subsequent gradual reduction in the Dirac voltage shift for 10pg/mL and 100pg/mL indicate a reduction in the number of available binding sites (anti-Clusterin antibodies) on the GFET sensors. Thus, to the best of our knowledge, this is the first time such a characteristic curve (**Figure 11**, graph on the right) for Dirac voltage shift has been demonstrated for Clusterin detection using CVD single layer graphene field-effect transistors that may also broadly be expected for the detection of other molecular species. **Table 3** shows a variety of biosensing platforms and detection techniques in comparison with our results reported here using 4-PER and Dirac voltage shift techniques.

We also tested the three GFET sensors for their specificity by introducing a three-orders-of-magnitude higher concentration (compared to 100 pg/mL of Clusterin) hCG antigen at a

concentration of 100 ng/mL; data are presented in **Table 2 and 3** and a summary of the results are shown in **Figure 11**. The three sensors resulted in only an average of −6 ± 3% change in resistance, demonstrating the excellent specificity of our GFET sensors and the functionalisation protocols. These highly promising results demonstrate the potential of our graphene sensors as low-cost, repeatable, sensitive and specific detection platforms suitable for detecting a variety of other disease diagnosis. Our future work involves the development of a novel multiplexing platform exploiting the fact that these GFET sensors are generic transducers of biological events.

5. Conclusion

We have reported the fabrication, functionalisation and characterization of graphene FET sensors using Raman spectroscopy, four-probe electrical measurements and absorbance spectra using the highly collimated microbeam of Diamond B23 beamline for the detection of a prominent Alzheimer's disease protein biomarker, Clusterin. The fabrication and functionalisation protocols have enabled detection of Clusterin from 1 pg/mL to 100 pg/mL, with a limit-of-detection of ~300 fg/mL (4 fM) using 4-PER measurement technique. In contrast, a characteristic curve for the Dirac voltage shift with Clusterin concentration has also been demonstrated using back-gated I_D-V_G measurements, although the standard deviation of these results were relatively higher than the results from 4-PER measurements. The GFET sensors were also found to have a repeatable performance over an extensive range of functionalisation stages from bare to 100 pg/mL of Clusterin using 4-PER measurements. In addition, the sensors were found to be highly specific, showing only a −6 ± 3 % resistance change compared to 100 pg/mL of Clusterin when a three-orders-of-magnitude higher concentration of hCG was applied (100 ng/mL) to the GFET sensors. Future work includes deploying the sensors to detect a panel of biomarkers for the early detection of Alzheimer's disease (such as ApoE, Aβ, etc.) using a novel multiplexing platform we are currently developing, which will be reported in a future study. In addition, as the GFET sensors are generic transducers, we anticipate their future applications in a variety of other disease biomarker detection also, such as cancer and cardiovascular.

Conflicts of Interest: The authors declare no conflict of interest. The funders had no role in the design of the study; in the collection, analyses, or interpretation of data; in the writing of the manuscript, or in the decision to publish the results.

Author Contributions: Conceptualization, S.A.A.; methodology, S.A.A., T.B., C.H., S.D. and B.O.; software, B.O. and T.B.; validation, S.A.A., T.B., G.S., and J.C.; formal analysis, S.A.A.; data curation, S.A.A.; writing—original draft preparation, S.A.A and T.B.; writing—review and editing, All; supervision, S.A.A.; T.W., and P.D.; project administration, S.A.A; funding acquisition, S.A.A. All authors have read and agreed to the published version of the manuscript.

Funding: This research was funded by University of Plymouth (C.H.: GD105227-104, B.O'D.: GD110025-104), Diamond Light Source, DLS-SM24459-1 and EPSRC under contract number EP/M006301/1.

Acknowledgments: We acknowledge Jeremy Clark (Materials & Structures), University of Plymouth, for usage of the optical microscope and LG Electronics for the supply of CVD graphene test samples.

References.

Awan, S. A., Kibble, B. and Schurr, J. (March, 2011). "*Coaxial Electrical Circuits for Interference-Free Measurements*." IET, London, UK: 334.

Awan, S. A., Lombardo, A., Colli, A., Privitera, G., Kulmala, T. S., Kivioja, J. M., et al. (2016). "Transport conductivity of graphene at RF and microwave frequencies." 2D Materials 3: 015010.

Baek, Y.-K., Jung, D.-H., Yoo, S. M., Shin, S., Kim, J.-H., Jeon, H.-J., et al. (2011). "Label-free detection of DNA hybridization using pyrene-functionalized single-walled carbon nanotubes: effect of chemical structures of pyrene molecules on DNA sensing performance." Journal of nanoscience and nanotechnology 11(5): 4210-4216.

Balandin, A. A., Ghosh, S., Bao, W., Calizo, I., Teweldebrhan, D., Miao, F., et al. (2008). "Superior Thermal Conductivity of Single-Layer Graphene." Nano Lett 8(3): 902-907.

Bao, Q. and Loh, K. P. (2012). "Graphene photonics, plasmonics, and broadband optoelectronic devices." ACS nano 6(5): 3677-3694.

Tips for reducing ELISA background (2012) https://www.biocompare.com/Bench-Tips/122704-Tips-for-Reducing-ELISA-Background/. [Accessed 12 October 2020]

Blake, P., Brimicombe, P. D., Nair, R. R., Booth, T. J., Jiang, D., Schedin, F., et al. (2008). "Graphene-Based Liquid Crystal Device." Nano Lett 8(6): 1704-1708.

Bøggild, P., Mackenzie, D. M. A., Whelan, P. R., Petersen, D. H., Buron, J. D., Zurutuza, A., et al. (2017). "Mapping the electrical properties of large-area graphene." 2D Materials 4(4).

Bolotin, K. I., Sikes, K. J., Jiang, Z., Klima, M., Fudenberg, G., Hone, J., et al. (2008). "Ultrahigh electron mobility in suspended graphene." Solid State Communications 146(9-10): 351-355.

Booth, T. J., Blake, P., Nair, R. R., Jiang, D., Hill, E. W., Bangert, U., et al. (2008). "Macroscopic Graphene Membranes and Their Extraordinary Stiffness." Nano Lett 8(8): 2442-2446.

Bunch, J. S., van der Zande, A. M., Verbridge, S. S., Frank, I. W., Tanenbaum, D. M., Parpia, J. M., et al. (2007). "Electromechanical resonators from graphene sheets." Science 315(5811): 490-493.

Calizo, I., Balandin, A., Bao, W., Miao, F. and Lau, C. (2007). "Temperature dependence of the Raman spectra of graphene and graphene multilayers." Nano letters 7(9): 2645-2649.

Casiraghi, C., Pisana, S., Novoselov, K., Geim, A. K. and Ferrari, A. (2007). "Raman fingerprint of charged impurities in graphene." Applied Physics Letters 91(23): 233108.

Castro Neto, A. H., Guinea, F., Peres, N. M. R., Novoselov, K. and A., G. (2009). "The Electronic Properties of Graphene." Rev. Mod. Phys. 81: 109-162.

Cheng, Z., Zhou, Q., Wang, C., Li, Q., Wang, C. and Fang, Y. (2011). "Toward intrinsic graphene surfaces: a systematic study on thermal annealing and wet-chemical treatment of SiO2-supported graphene devices." Nano Lett 11(2): 767-771.

Chun, L., Kim, S.-E., Cho, M., Choe, W.-s., Nam, J., Lee, D. W., et al. (2013). "Electrochemical detection of HER2 using single stranded DNA aptamer modified gold nanoparticles electrode." Sensors and Actuators B: Chemical 186: 446-450.

Mayo clinic: Dementia. (2020) https://www.mayoclinic.org/diseases-conditions/dementia/diagnosis-treatment/drc-20352019. [Accessed 09 September 2020]

Cui, Z., Wu, D., Zhang, Y., Ma, H., Li, H., Du, B., et al. (2014). "Ultrasensitive electrochemical immunosensors for multiplexed determination using mesoporous platinum nanoparticles as nonenzymatic labels." Analytica chimica acta 807: 44-50.

Damiati, S., Haslam, C., Søpstad, S., Peacock, M., Whitley, T., Davey, P., et al. (2019). "Sensitivity comparison of macro-and micro-electrochemical biosensors for human chorionic gonadotropin (hCG) biomarker detection." IEEE Access 7: 94048-94058.

De Silva, H., Stuart, W. D., Duvic, C., Wetterau, J. R., Ray, M. J., Ferguson, D., et al. (1990). "A 70-kDa apolipoprotein designated ApoJ is a marker for subclasses of human plasma high density lipoproteins." Journal of Biological Chemistry 265(22): 13240-13247.

Dong, X., Shi, Y., Huang, W., Chen, P. and Li, L. J. (2010). "Electrical detection of DNA hybridization with single-base specificity using transistors based on CVD-grown graphene sheets." Adv Mater 22(14): 1649-1653.

Ferrari, A. C. (2007). "Raman spectroscopy of graphene and graphite: Disorder, electron–phonon coupling, doping and nonadiabatic effects." Solid state communications 143(1-2): 47-57.

Ferrari, A. C., Meyer, J. C., Scardaci, V., Casiraghi, C., Lazzeri, M., Mauri, F., et al. (2006). "Raman spectrum of graphene and graphene layers." Phys Rev Lett 97(18): 187401.

Geim, A. K. and Novoselov, K. S. (2010). The rise of graphene. Nanoscience and technology: a collection of reviews from nature journals, World Scientific, 11-19.

Ghiso, J., Matsubara, E., Koudinov, A., Choi-Miura, N. H., Tomita, M., Wisniewski, T., et al. (1993). "The cerebrospinal-fluid soluble form of Alzheimer's amyloid β is complexed to SP-40, 40 (apolipoprotein J), an inhibitor of the complement membrane-attack complex." Biochemical Journal 293(1): 27-30.

Glenner, G. G. and Wong, C. W. (1984). "Alzheimer's disease: Initial report of the purification and characterization of a novel cerebrovascular amyloid protein " Biochim Biophys Res Comms 120(3): 885-890.

Graf, D., Molitor, F., Ensslin, K., Stampfer, C., Jungen, A., Hierold, C., et al. (2007). "Spatially resolved Raman spectroscopy of single-and few-layer graphene." Nano letters 7(2): 238-242.

Hardy, J. and Selkoe, D. J. (2002). "The Amyloid Hypothesis of Alzheimer's Disease Progress on the Road to Therapeutics." Science 297: 353-356.

Haslam, C., Damiati, S., Whitley, T., Davey, P., Ifeachor, E. and Awan, S. A. (2018). "Label-Free Sensors Based on Graphene Field-Effect Transistors for the Detection of Human Chorionic Gonadotropin Cancer Risk Biomarker." Diagnostics (Basel) 8(1).

Hill, A. V., (1910). "The combinations of haemoglobin with oxygen and with carbon monoxide." I. J. Physiol.40, iv-vii.

Huang, M., Yan, H., Chen, C., Song, D., Heinz, T. F. and Hone, J. (2009). "Phonon softening and crystallographic orientation of strained graphene studied by Raman spectroscopy." Proceedings of the National Academy of Sciences 106(18): 7304-7308.

Huang, Y., Dong, X., Liu, Y., Li, L.-J. and Chen, P. (2011). "Graphene-based biosensors for detection of bacteria and their metabolic activities." Journal of Materials Chemistry 21(33): 12358-12362.

Hussain, R., Jávorfi, T. and Siligardi, G. (2012). "Circular dichroism beamline B23 at the Diamond Light Source." Journal of synchrotron radiation 19(1): 132-135.

Iqbal, K., Alonso Adel, C., Chen, S., Chohan, M. O., El-Akkad, E., Gong, C. X., et al. (2005). "Tau pathology in Alzheimer disease and other tauopathies." Biochim Biophys Acta 1739(2-3): 198-210.

Islam, K., Damiati, S., Sethi, J., Suhail, A. and Pan, G. (2018). "Development of a Label-Free Immunosensor for Clusterin Detection as an Alzheimer's Biomarker." Sensors (Basel) 18(1).

James, R., Hochstrasser, A., Borghini, I., Martin, B., Pometta, D. and Hochstrasser, D. (1991). "Characterization of a human high density lipoprotein-associated protein, NA1/NA2. Identity with SP-40, 40, an inhibitor of complement-mediated cytolysis." Arteriosclerosis and thrombosis: a journal of vascular biology 11(3): 645-652.

Justino, C. I. L., Gomes, A. R., Freitas, A. C., Duarte, A. C. and Rocha-Santos, T. A. P. (2017). "Graphene based sensors and biosensors." TrAC Trends in Analytical Chemistry 91: 53-66.

Kirszbaum, L., Bozas, S. and Walker, I. (1992). "SP-40, 40, a protein involved in the control of the complement pathway, possesses a unique array of disulphide bridges." FEBS letters 297(1-2): 70-76.

Kumar, K., Kim, Y.-S. and Yang, E.-H. (2013). "The influence of thermal annealing to remove polymeric residue on the electronic doping and morphological characteristics of graphene." Carbon 65: 35-45.

Langmuir, I. (1918). "The adsorption of gases on plane surfaces of glass, mica and platinum." J. Am. Chem. Soc. 40 (9): 1361-1403.

Leva-Bueno, J., Peyman, S. A., Millner, P. A. (2020). " A review on impedimetric immunosensors for pathogen and biomarker detection." Medical Microbiology and Immunology, 209: 243-362.

Lidström, A., Bogdanovic, N., Hesse, C., Volkman, I., Davidsson, P. and Blennow, K. (1998). "Clusterin (apolipoprotein J) protein levels are increased in hippocampus and in frontal cortex in Alzheimer's disease." Experimental neurology 154(2): 511-521.

Lin, Y.-M., Dimitrakopoulos, C., Jenkins, K. A., Farmer, D. B., Chiu, H.-Y., Grill, A., et al. (2010). "100-GHz transistors from wafer-scale epitaxial graphene." Science 327(5966): 662-662.

Lin, Y. C., Lu, C. C., Yeh, C. H., Jin, C., Suenaga, K. and Chiu, P. W. (2012). "Graphene annealing: how clean can it be?" Nano Lett 12(1): 414-419.

Mafra, D., Samsonidze, G., Malard, L., Elias, D. C., Brant, J., Plentz, F., et al. (2007). "Determination of LA and TO phonon dispersion relations of graphene near the Dirac point by double resonance Raman scattering." Physical Review B 76(23): 233407.

Masters, C. L., Simm, G., Weinman, N. A., Multhaup, G., Mcdonald, B. L. and B., K. (1985). "Amyloid plaque core protein in Alzheimer disease and down syndrome." Proc. Natl. Acad. Sci. 82: 4245-4249.

Matsubara, E., Soto, C., Governale, S., Frangione, B. and Ghiso, J. (1996). "Apolipoprotein J and Alzheimer's amyloid β solubility." Biochemical Journal 316(2): 671-679.

May, P. C., Lampert-Etchells, M., Johnson, S. A., Poirier, J., Masters, J. N. and Finch, C. E. (1990). "Dynamics of gene expression for a hippocampal glycoprotein elevated in Alzheimer's disease and in response to experimental lesions in rat." Neuron 5(6): 831-839.

Morozov, S. V., Novoselov, K. S., Katsnelson, M. I., Schedin, F., Elias, D. C., Jaszczak, J. A., et al. (2008). "Giant Intrinsic Carrier Mobilities in Graphene and Its Bilayer.pdf." Phys. Rev. lett. 100: 11-14.

Novoselov, K. S., Geim, A., K.Morozov, S. V., Jiang, D., Zhang, Y., Dubonos, S. V., et al. (2004). "Electric Field Effect in Atomically Thin Carbon Films." Science 306(30): 666-669.

Novoselov, K. S., Geim, A. K., Morozov, S. V., Jiang, D., Katsnelson, M. I., Grigorieva, I. V., et al. (2005). "Two-dimensional gas of massless Dirac fermions in graphene." Nature 438(7065): 197-200.

Novoselov, K. S., Jiang, D., Schedin, F., Booth, T. J., Khotkevich, V. V., Morozov, S. V., et al. (2005). "Two-dimensional Atomic Crystals." Proceedings of National Academy of Sciences 102(5696): 10451-10453.

Oda, T., Pasinetti, G., Osterburg, H., Anderson, C., Johnson, S. and Finch, C. (1994). "Purification and characterization of brain clusterin." Biochemical and biophysical research communications 204(3): 1131-1136.

Okamoto, S., Ohno, Y., Maehashi, K., Inoue, K. and Matsumoto, K. (2012). "Immunosensors Based on Graphene Field-Effect Transistors Fabricated Using Antigen-Binding Fragment." Japanese Journal of Applied Physics 51.

Pawula, M., Altintas, Z. and Tothill, I. E. (2016). "SPR detection of cardiac troponin T for acute myocardial infarction." Talanta 146: 823-830.

Pirkle, A., Chan, J., Venugopal, A., Hinojos, D., Magnuson, C. W., McDonnell, S., et al. (2011). "The effect of chemical residues on the physical and electrical properties of chemical vapor deposited graphene transferred to SiO2." Applied Physics Letters 99(12).

Rama, E. C., González-García, M. B. and Costa-Garcia, A. (2014). "Competitive electrochemical immunosensor for amyloid-beta 1-42 detection based on gold nanostructurated Screen-Printed Carbon Electrodes." Sensors and Actuators B: Chemical 201: 567-571.

Satapathy, S. (2017). "Extracellular chaperones in neuronal proteinopathies: protecting and facilitating neuronal function." Cell Communication Insights 9: 1-13.

Schrijvers, E. M., Koudstaal, P. J., Hofman, A. and Breteler, M. M. (2011). "Plasma clusterin and the risk of Alzheimer disease." Jama 305(13): 1322-1326.

Schürmann, B., Wiese, B., Bickel, H., Weyerer, S., Riedel-Heller, S. G., Pentzek, M., et al. (2011). "Association of the Alzheimer's disease clusterin risk allele with plasma clusterin concentration." Journal of Alzheimer's Disease 25(3): 421-424.

Selkoe, D. J. (1991). The molecular pathology of Alzheimer's disease, Neuron. 6, 487-498.

Alzheimer's Society: Facts for the media. (2020) https://www.alzheimers.org.uk/about-us/news-and-media/facts-media. [Accessed 09 September 2020]

Stankovich, S., Dikin, D. A., Dommett, G. H., Kohlhaas, K. M., Zimney, E. J., Stach, E. A., et al. (2006). "Graphene-based composite materials." nature 442(7100): 282-286.

Teixeira, S., Burwell, G., Castaing, A., Gonzalez, D., Conlan, R. & Guy, O. (2014). "Epitaxial graphene immunosensor for human chorionic gonadotropin." Sensors and Actuators B: Chemical, 190: 723-729.

Thambisetty, M., An, Y., Kinsey, A., Koka, D., Saleem, M., Güntert, A., et al. (2012). "Plasma clusterin concentration is associated with longitudinal brain atrophy in mild cognitive impairment." Neuroimage 59(1): 212-217.

Thambisetty, M., Simmons, A., Velayudhan, L., Hye, A., Campbell, J., Zhang, Y., et al. (2010). "Association of plasma clusterin concentration with severity, pathology, and progression in Alzheimer disease." Archives of general psychiatry 67(7): 739-748.

Tsang, D. K. H., Lieberthal, T. J., Watts, C., Dunlop, I. E., Ramadan, S., Hernandez, A. E. D. R. Klein, N. (2019). "Chemically functionalised graphene FET biosensors for the label-free sensing of exosomes", Scientific Reports, 9:13946.

Tsuruta, J., Wong, K., Fritz, I. and Griswold, M. (1990). "Structural analysis of sulphated glycoprotein 2 from amino acid sequence. Relationship to clusterin and serum protein 40, 40." Biochemical Journal 268(3): 571-578.

Uludag, Y. and Tothill, I. E. (2012). "Cancer biomarker detection in serum samples using surface plasmon resonance and quartz crystal microbalance sensors with nanoparticle signal amplification." Analytical chemistry 84(14): 5898-5904.

Vu, C. A. and Chen, W. Y. (2019). "Field-Effect Transistor Biosensors for Biomedical Applications: Recent Advances and Future Prospects." Sensors (Basel) 19(19): 4212-4222.

Wang, X., Zhi, L. and Mullen, K. (2008). "Transparent, Conductive Graphene Electrodes for Dye-Sensitized Solar Cells." Nano Lett 8(1): 323-327.

Wang, Y., Shi, Z., Huang, Y., Ma, Y., Wang, C., Chen, M., et al. (2009). "Supercapacitor Devices Based on Graphene Materials." J Phys Chem C 113: 13103-13107.

Wu, C.-C., Ku, B.-C., Ko, C.-H., Chiu, C.-C., Wang, G.-J., Yang, Y.-H., et al. (2014). "Electrochemical impedance spectroscopy analysis of A-beta (1-42) peptide using a nanostructured biochip." Electrochimica Acta 134: 249-257.

Wu, W.-Y., Bian, Z.-P., Wang, W. and Zhu, J.-J. (2010). "PDMS gold nanoparticle composite film-based silver enhanced colorimetric detection of cardiac troponin I." Sensors and Actuators B: Chemical 147(1): 298-303.

Zhong, H., Zhang, Z., Xu, H., Qiu, C. and Peng, L.-M. (2015). "Comparison of mobility extraction methods based on field-effect measurements for graphene." AIP Advances 5(5).

Zupančič, U., Jolly, P., Estrela P., Moschou, D., Ingber, D. E. (2021). " Graphene Enabled Low-Noise Surface Chemistry for Multiplexed Sepsis Biomarker Detection in Whole Blood." Advanced Functional Materials, 2010638.

Figures and Tables

Figure 1:

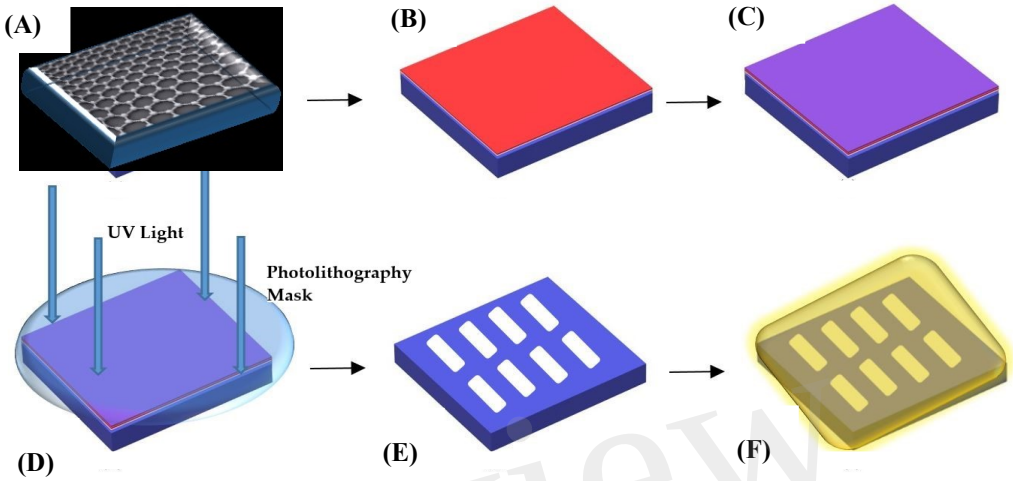

Figure 1. Overview of the processes for GFET fabrication **(A)** layer of graphene on Si/SiO_2 substrate **(B)** LoR deposition **(C)** PR deposition **(D)** sample below the photolithography mask aligner for UV exposure **(E)** etching of graphene channels and chemical developing process **(F)** final stage of metallic Cr and Au deposition

Figure 2:

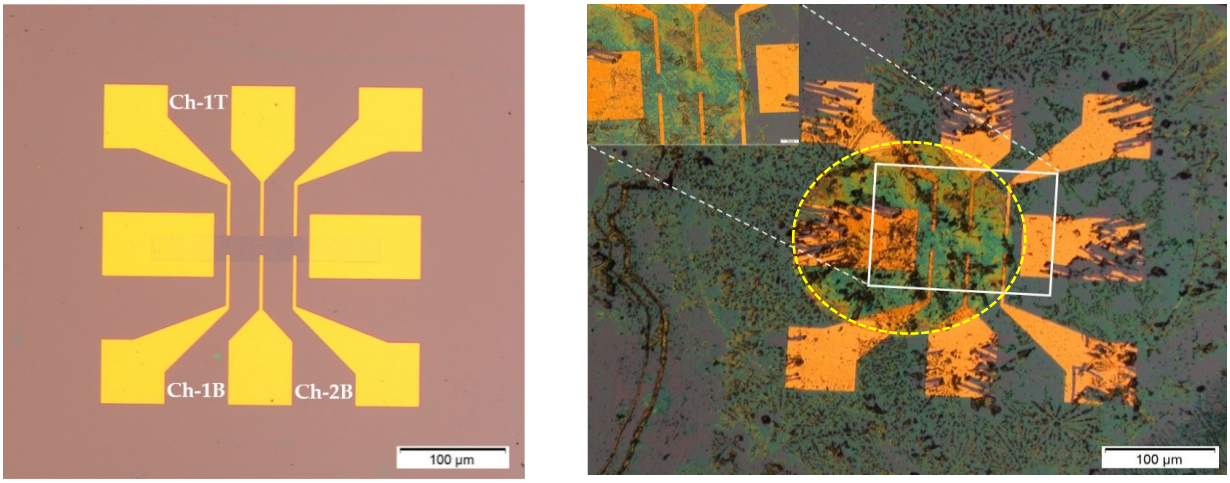

(A) **(B)**

Figure 2. Graphene field effect transistor (GFET) devices; **(A)** symmetric GFET device with graphene channel length of 400 µm (symmetry by 3 voltage leads above and below the graphene channel). Here Ch-1T refers to channel 1 top voltage leads, Ch-lB refers to channel 1 bottom voltage leads and Ch-2B refers to channel 2 bottom voltage leads; **(B)** functionalised symmetric GFET device Clusterin (1pg/mL) with zoomed in inset of graphene channel and yellow dotted lines indicating the drop of solutions on the two series GFET channels (diameter of the drop region is ~900 µm).

Figure 3:

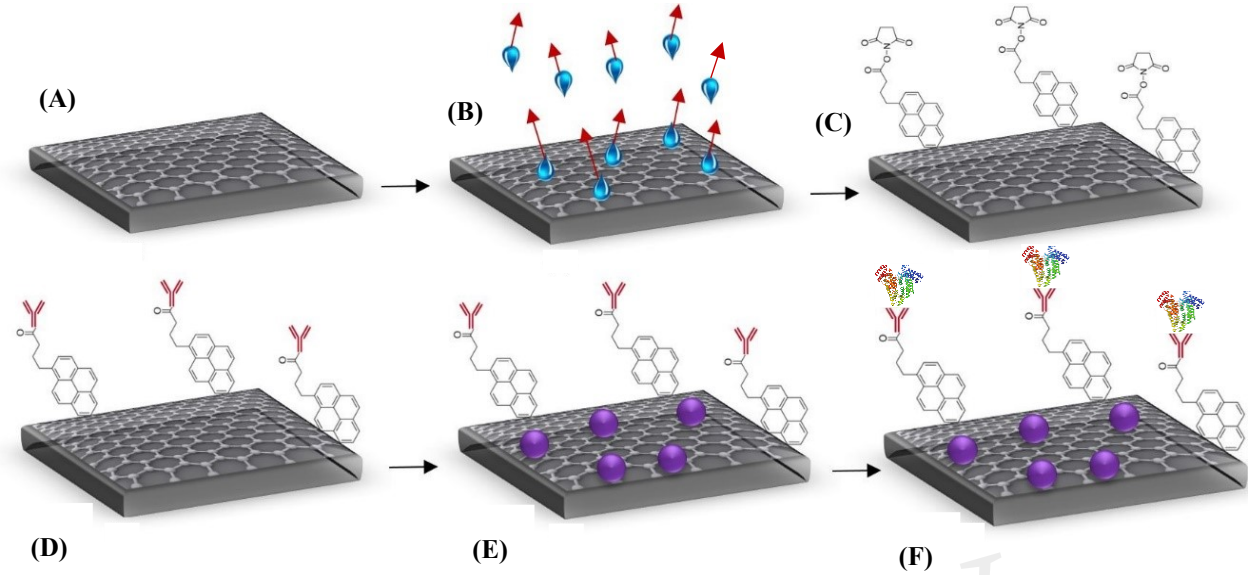

Figure 3. Steps for GFET functionalisation **(A)** bare graphene **(B)** annealed graphene (showing evaporation of water molecules) **(C)** attachment of Pyr-NHS ester molecules with graphene **(D)** anti-Clusterin antibody attachment to linkers (red) **(E)** BSA blocking (purple) and **(F)** binding of Clusterin (tri-colour molecules) with the anti-Clusterin antibody

Figure 4:

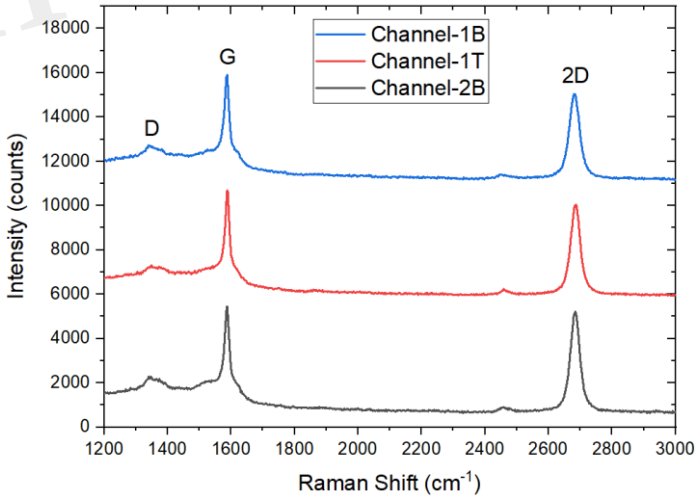

Figure 4. Raman Spectra of three monolayer graphene field-effect transistor (GFET) sensors after fabrication.

Figure 5:

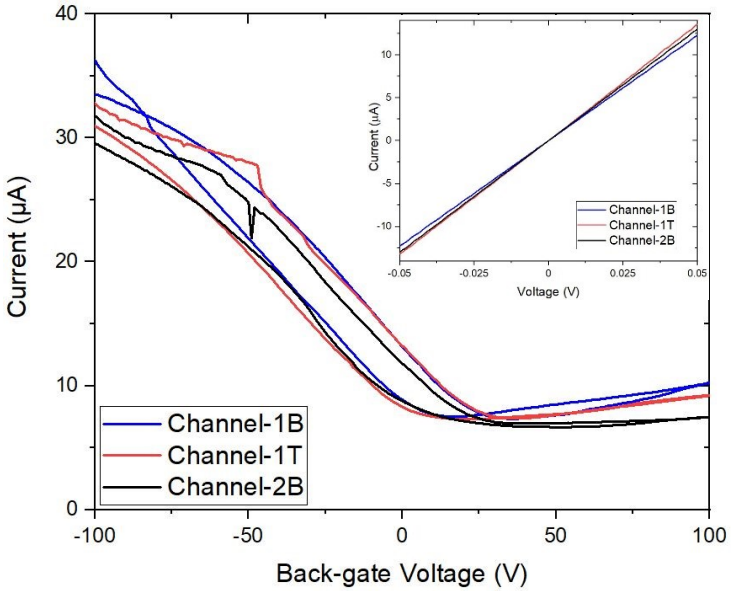

Figure 5. Characteristic transfer curve I_D–V_G measurements of three graphene channels with corresponding output I_D–V_D curves (inset). Back-gated measurements showing forward and reverse sweep (from −100 V to 100 V) demonstrate the bare graphene channels are electrically almost identical.

Figure 6:

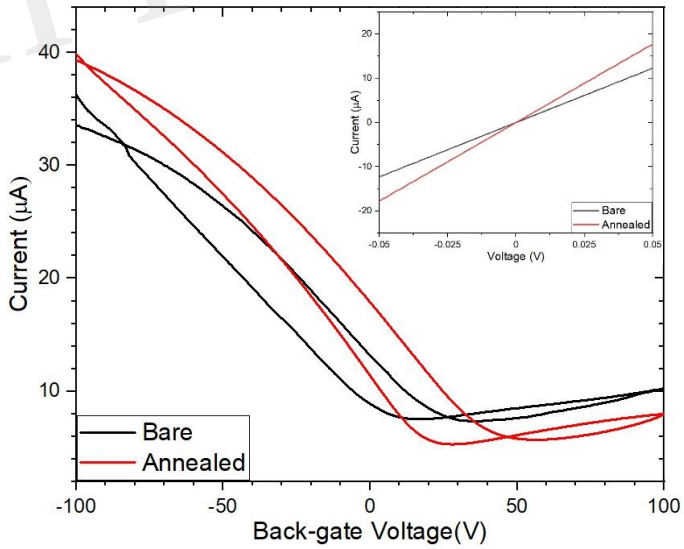

Figure 6. Comparison of the bare and annealed I_D–V_G curves with their corresponding I_D–V_D curves (inset).

Figure 7:

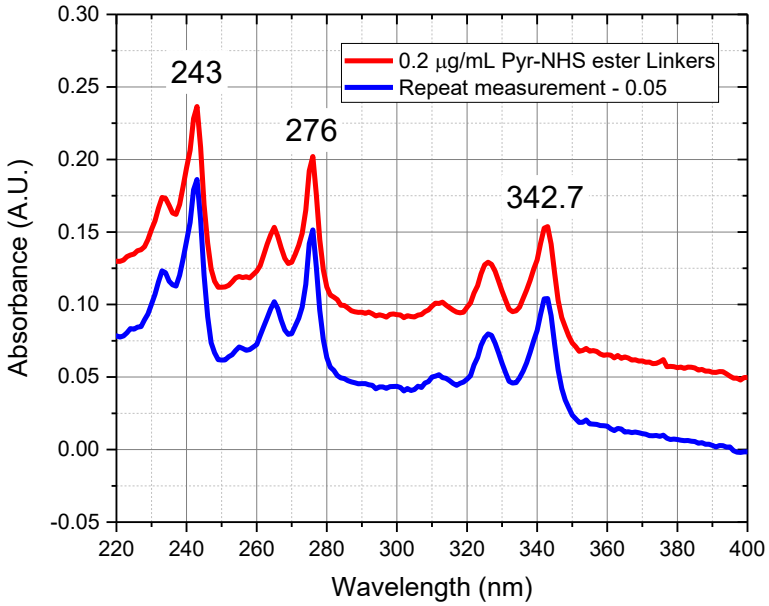

Figure 7. Absorbance spectra of Pyr-NHS ester linker molecules at 0.2 µg/mL concentration (red curve) and a repeat measurement (blue curve) off-set by 0.05 for clarity, showing the characteristic triple peaks due to the presence of pyrene moiety.

Figure 8:

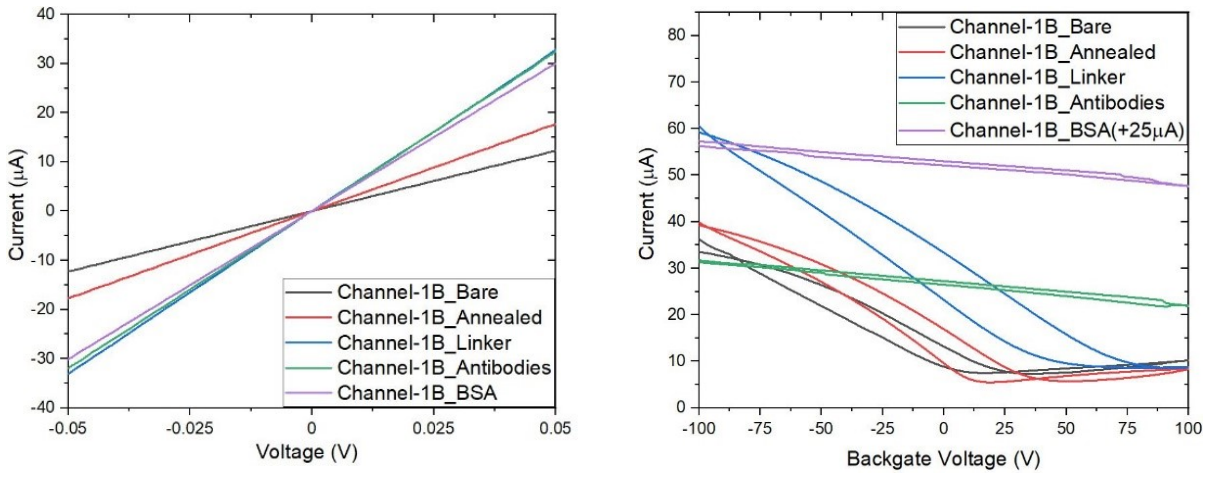

(A) **(B)**

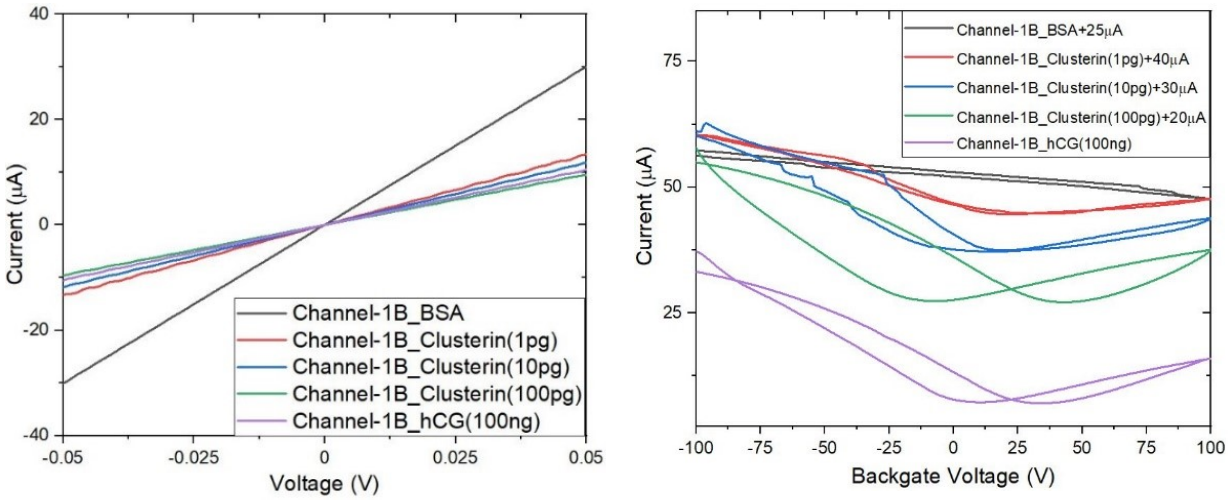

(C) **(D)**

Figure 8. Characteristic curves for Channel-1B **(A)** I_D–V_D output curves for bare to BSA **(B)** I_D–V_G transfer curves for bare to BSA **(C)** I_D–V_D curves for BSA to human chorionic gonadotropin (hCG) (100ng) and **(D)** I_D–V_G curves for BSA to hCG (100ng) with off-set currents shown for clarity. Antigen concentrations are in units of g/mL.

Figure 9:

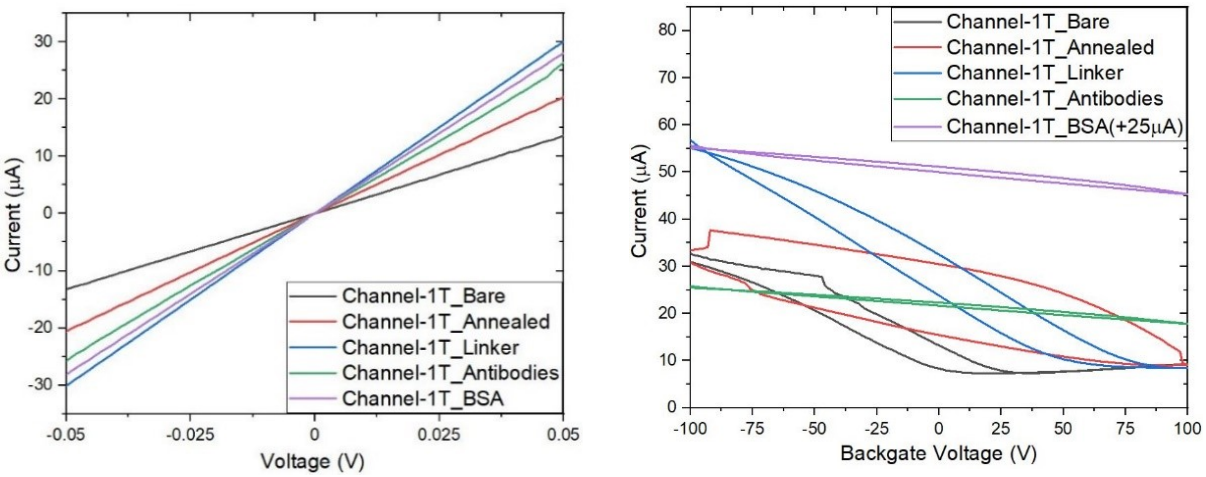

(A) **(B)**

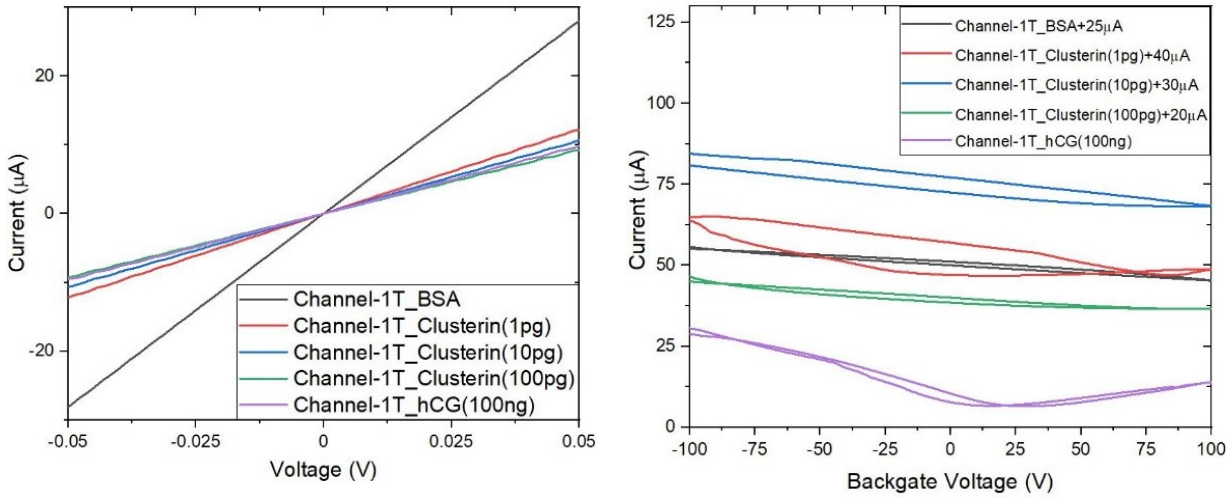

(C) **(D)**

Figure 9. Characteristic curves for Channel-1T **(A)** I_D–V_D output curves for bare to BSA **(B)** I_D–V_G transfer curves for bare to BSA **(C)** I_D–V_D curves for BSA to hCG (100 ng/mL) and **(D)** I_D–V_G curves for BSA to hCG (100 ng/mL), with off-set currents shown for clarity. Antigen concentrations are in units of g/mL.

Figure 10:

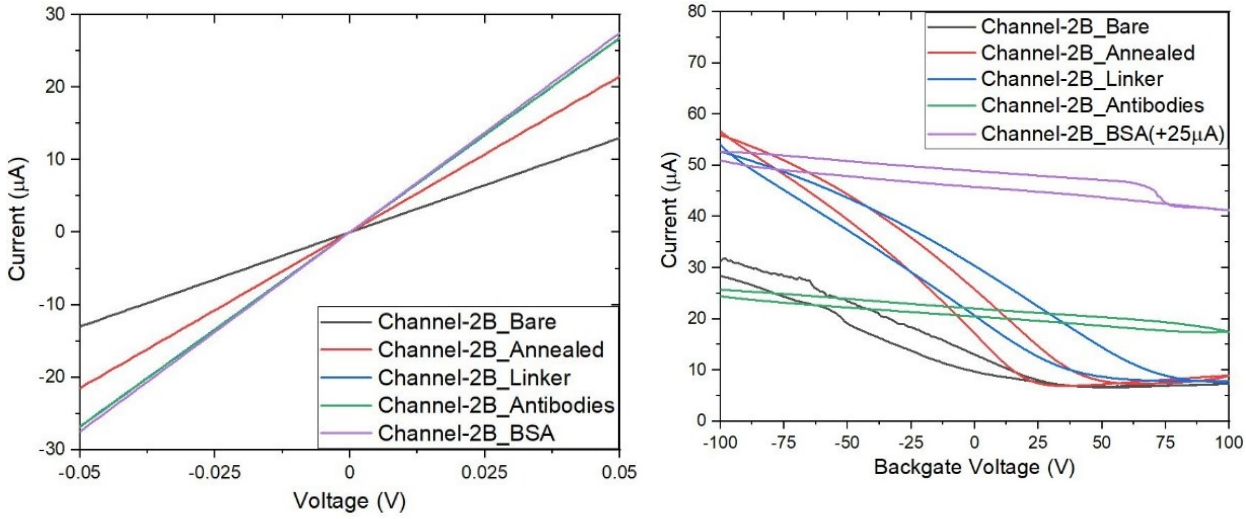

(A) **(B)**

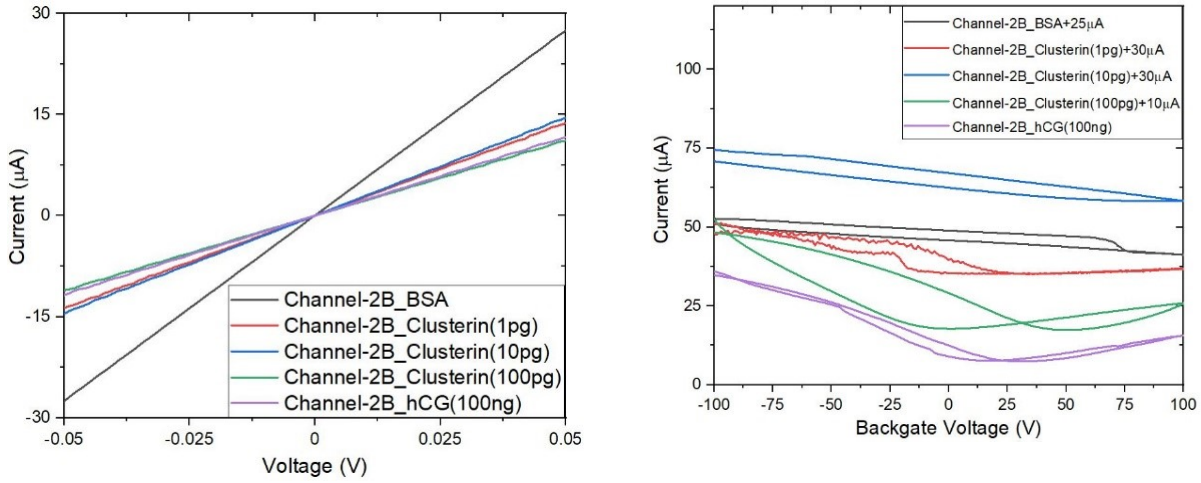

(C) **(D)**

Figure 10. Characteristic curves for Channel-2B **(A)** I_D–V_D output curve for bare to BSA **(B)** I_D–V_G transfer curve for bare to BSA **(C)** I_D–V_D curve for BSA to hCG (100 ng/mL) and **(D)** I_D–V_G curve for BSA to hCG (100 ng/mL), with off-set currents shown for clarity. Antigen concentrations are in units of g/mL.

Figure 11:

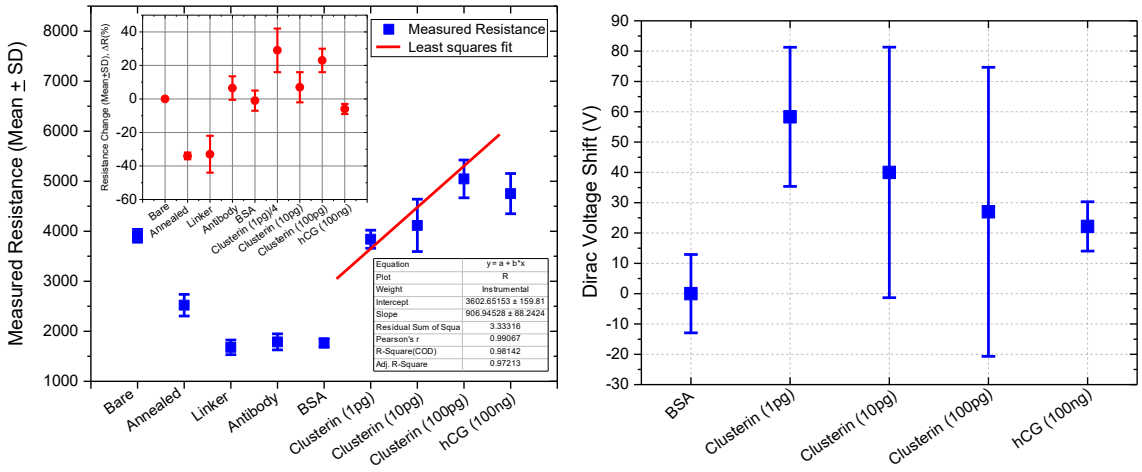

Figure 11. Measured resistance (Mean ±SD) for each functionalization stage with a log-linear least squares fit (solid line, effectively a partial Hill-Langmuir equation fit) to the measured data from 1pg/mL to 100pg/mL of Clusterin concentration and the fit parameters showing adjusted $r^2 \sim 0.98$ (Left). The inset shows corresponding percentage resistance change relative to the previous stage (with bare stage being 0% by definition). Note, the data in the inset for resistance change at 1pg/mL Clusterin is reduced by a factor of 4 for clarity and analyte concentrations are in units of g/mL. Corresponding back-gated measurements of Dirac voltage shifts normalized with respect to the BSA stage (right).

Table 1. The forward and reverse Dirac point voltages (DPV) and the resistance of the three channels. The Dirac point voltages reveal that the GFET is p-doped. Back-gate sweep rate was ~ 20V/s.

Channel	Forward Sweep DCV	Reverse Sweep DCV	Resistance
Channel-1B	17 V	35 V	4086 Ω
Channel-1T	35 V	22 V	3789 Ω
Channel-2B	42 V	51 V	3852 Ω

Table 2. The raw resistance and resistance change (%) for Bare to BSA stages of functionalisation for the three channels and the corresponding mean and standard deviation values. The percentage changes are calculated for the two nearest stages (i.e. Bare to Annealed, Annealed to Linker etc.)

Channel	Bare (Ω)	Annealed (Ω)	ΔR (%)	Linker (Ω)	ΔR (%)	Antibodies (Ω)	ΔR (%)	BSA (Ω)	ΔR (%)
Channel-1B	4086	2822	−31	1509	−47	1566	+3.8	1660	+6
Channel-1T	3789	2422	−36	1660	−31	1936	+16	1775	−8
Channel-2B	3852	2323	−35	1868	−20	1862	−0.3	1862	−2.4
Mean ± SD	3909 ± 128	2522 ± 216	−34 ± 2	1679 ± 147	−33 ± 11	1788 ± 160	6.5 ± 7	1766 ± 83	−1 ± 6

Table 3. The raw resistance and resistance change (%) for Clusterin (1pg/mL) to hCG (100ng/mL) stages of functionalisation for the three channels and the corresponding mean and standard deviation values. The Clusterin and hCG concentrations are in units of g/mL.

Channel	Clusterin (1pg) (Ω)	ΔR (%)	Clusterin (10pg) (Ω)	ΔR (%)	Clusterin (100pg) (Ω)	ΔR (%)	hCG (100ng) (Ω)	ΔR (%)
Channel-1B	3778	+127	4225	+11	5212	+23	4754	−9
Channel-1T	4084	+130	4697	+15	5406	+15	5244	−2
Channel-2B	3657	+101	3429	−6	4524	+32	4257	−6
Mean ± SD	3840 ± 180	117 ± 13	4117 ± 523	7 ± 9	5047 ± 378	23 ± 7	4752 ± 403	−6 ± 3

Table 4. Other approaches deployed for biosensors in comparison with our four-probe electrical detection technique.

Electrode Materials	Receptor System	Detection Technique	LoD (pg/mL)	Ref.
SPCE-NPAu	SPCE-NPAu/Streptavidin/Biotin-Aβ-42/anti-Aβ/anti-IgG-AP	CV	100	(Rama, González-García et al. 2014)
Gold Nanoparticles	GNP/MUA/NHS-EDC/Aβ(1-42) monoclonal antibody IgG/BSA/Aβ(1-42) peptide solution	EIS	1	(Wu, Ku et al. 2014)
SPCE/Carbon	SPCE/PANHS/Anti-hCG Ab/BSA/hCG	CV/Electrochemical	1	(Damiati, Haslam et al. 2019)
Au Nanoparticles	Au/PSA antibody/BSA/PSA/tPSA	SPR	30	(Uludag and Tothill 2012)
SPCE	SPCE/Pyr-NHS/anti-CLU F(ab')$_2$/BSA/CLU	CV/SWV	1	(Islam, Damiati et al. 2018)
SPR Chip-Gold	Gold film/EDC-NHS/anti-cTnT antibody/BSA/cTnT	SPR	500	(Pawula, Altintas et al. 2016)
Gold nanoparticles	Gold electrode/AuNP/MPA self-assembly/EDC-NHS/BSA/HER2	EIS	500	(Chun, Kim et al. 2013)
Graphite electrodes	Electrode/EDC-NHS/anti-CA125,anti-CA153,anti-CEA/BSA/CA125,CA153,CEA/M-Pt-CA125Ab$_2$,M-Pt-CA153 Ab$_2$,M-Pt-CEA Ab$_2$	DPV	7	(Cui, Wu et al. 2014)
PDMS/AuNP	PDMS/AuNP/anti-human IgG(cTnI)/BSA/human IgG(cTnI)	Colorimetric	10	(Wu, Bian et al. 2010)
GFET	Graphene/Pyr-NHS/anti-CLU/BSA/CLU	4-PER	0.3	This work

Figures and Tables

Figure 1:

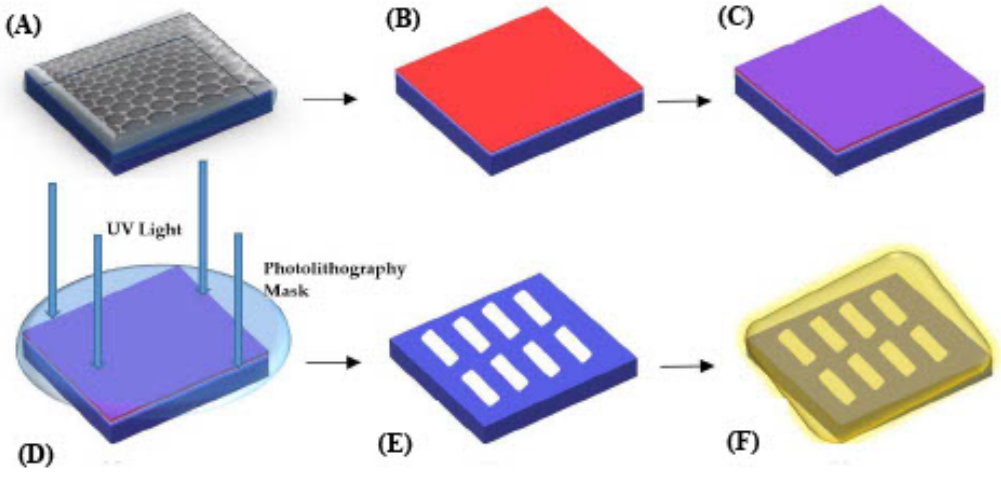

Figure 1. Overview of the processes for GFET fabrication **(A)** layer of graphene on Si/SiO_2 substrate **(B)** LoR deposition **(C)** PR deposition **(D)** sample below the photolithography mask aligner for UV exposure **(E)** etching of graphene channels and chemical developing process **(F)** final stage of metallic Cr and Au deposition

Figure 2:

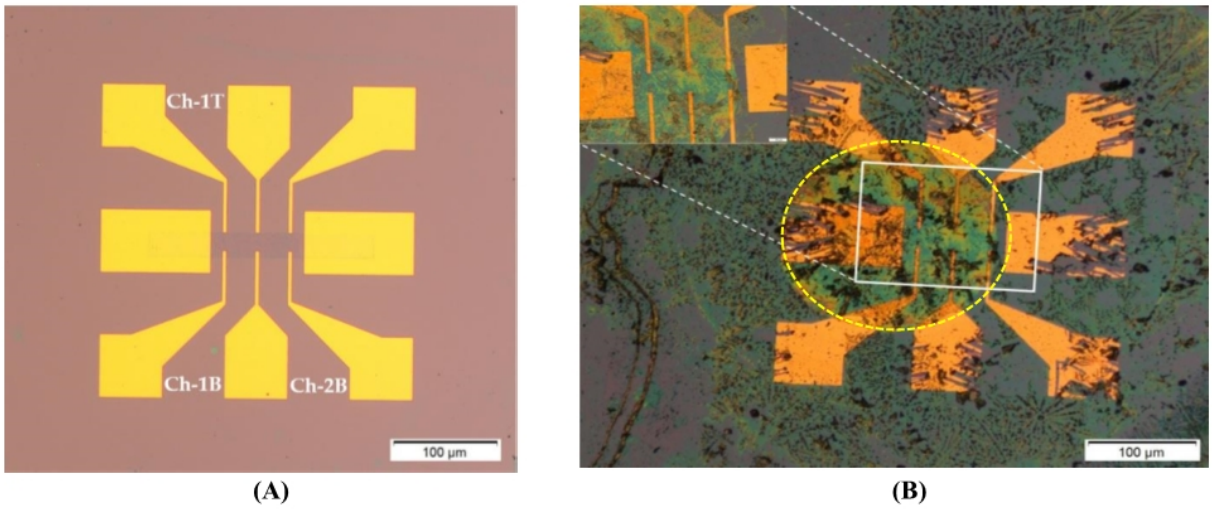

(A) **(B)**

Figure 2. Graphene field effect transistor (GFET) devices; **(A)** symmetric GFET device with graphene channel length of 400 µm (symmetry by 3 voltage leads above and below the graphene channel). Here Ch-1T refers to channel 1 top voltage leads, Ch-lB refers to channel 1 bottom voltage leads and Ch-2B refers to channel 2 bottom voltage leads; **(B)** functionalised symmetric GFET device Clusterin (1pg/mL) with zoomed in inset of graphene channel and yellow dotted lines indicating the drop of solutions on the two series GFET channels (diameter of the drop region is ~900 µm).

Figure 3:

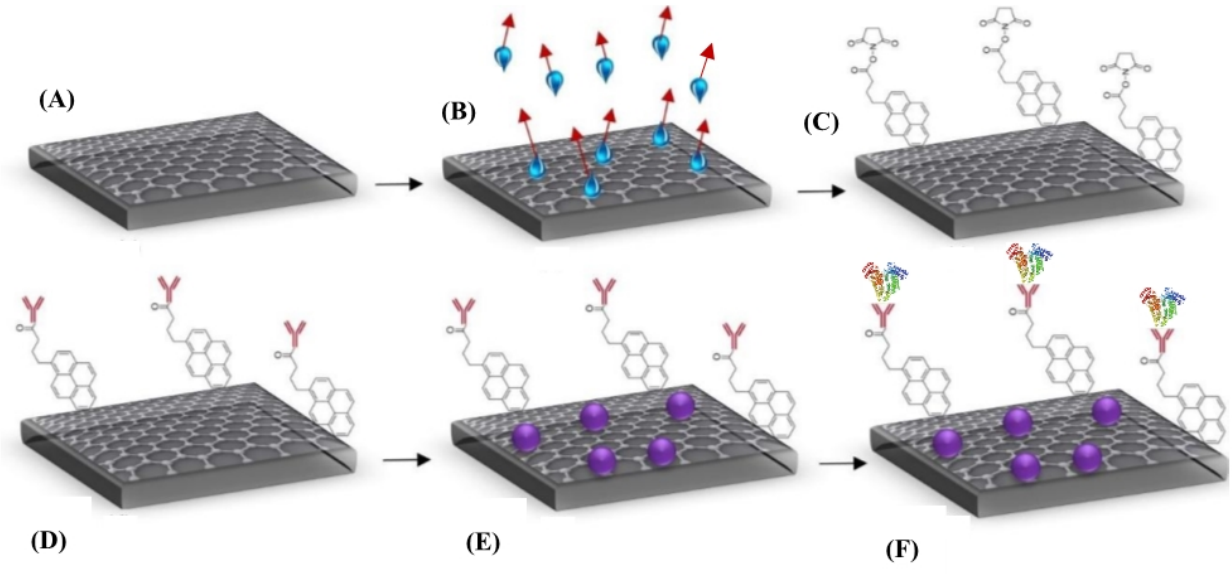

Figure 3. Steps for GFET functionalisation **(A)** bare graphene **(B)** annealed graphene (showing evaporation of water molecules) **(C)** attachment of Pyr-NHS ester molecules with graphene **(D)** anti-Clusterin antibody attachment to linkers (red) **(E)** BSA blocking (purple) and **(F)** binding of Clusterin (tri-colour molecules) with the anti-Clusterin antibody

Figure 4:

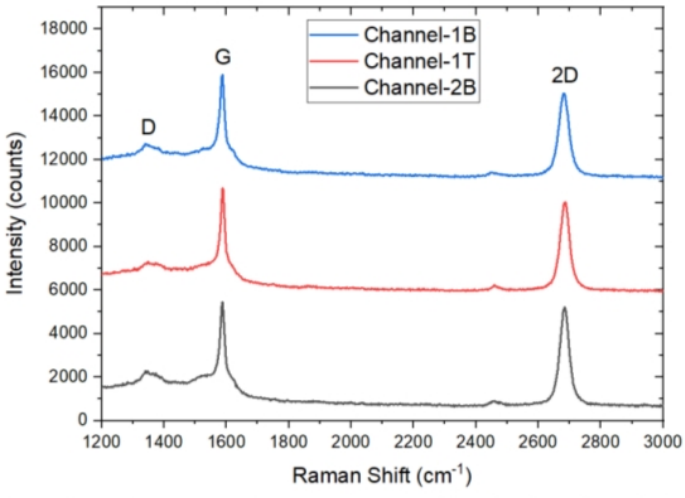

Figure 4. Raman Spectra of three monolayer graphene field-effect transistor (GFET) sensors after fabrication.

Figure 5:

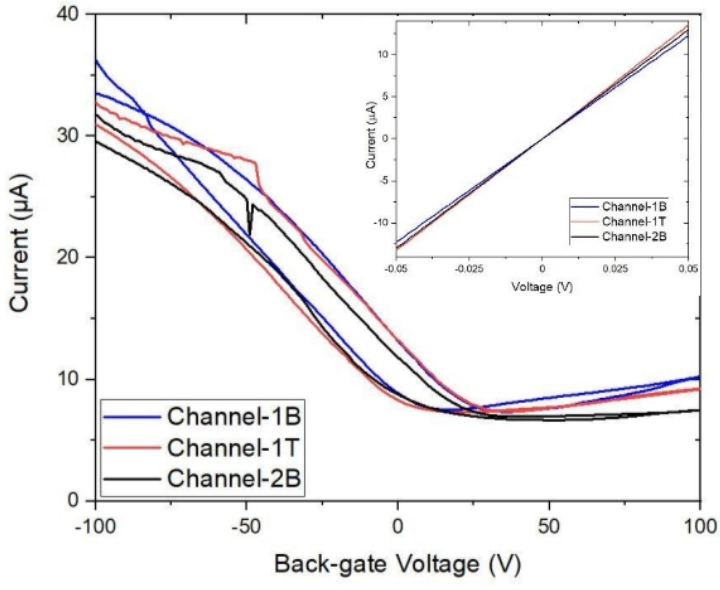

Figure 5. Characteristic transfer curve I_D–V_G measurements of three graphene channels with corresponding output I_D–V_D curves (inset). Back-gated measurements showing forward and reverse sweep (from −100 V to 100 V) demonstrate the bare graphene channels are electrically almost identical.

Figure 6:

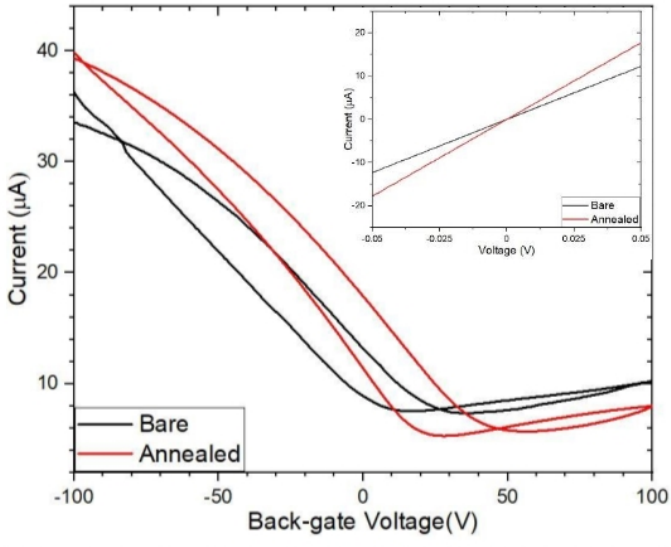

Figure 6. Comparison of the bare and annealed I_D–V_G curves with their corresponding I_D–V_D curves (inset).

Figure 7:

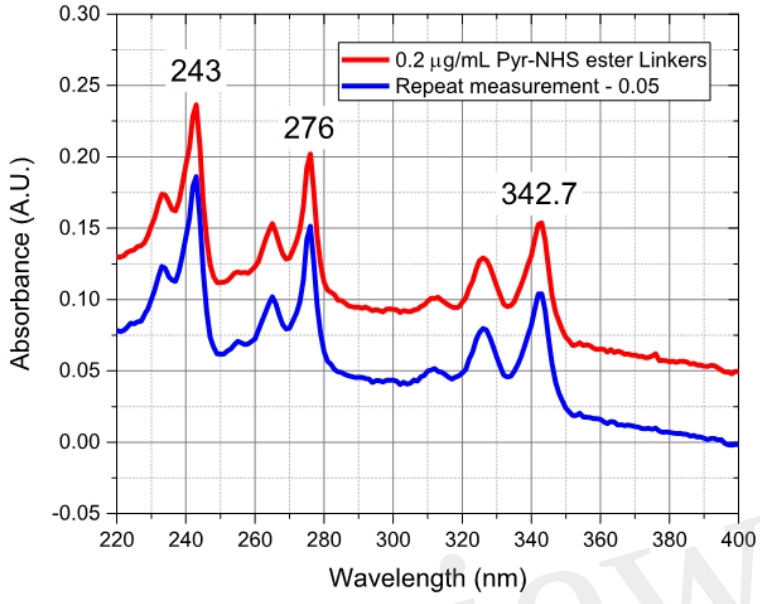

Figure 7. Absorbance spectra of Pyr-NHS ester linker molecules at 0.2 µg/mL concentration (red curve) and a repeat measurement (blue curve) off-set by 0.05 for clarity, showing the characteristic triple peaks due to the presence of pyrene moiety.

frontiers

Figure 8:

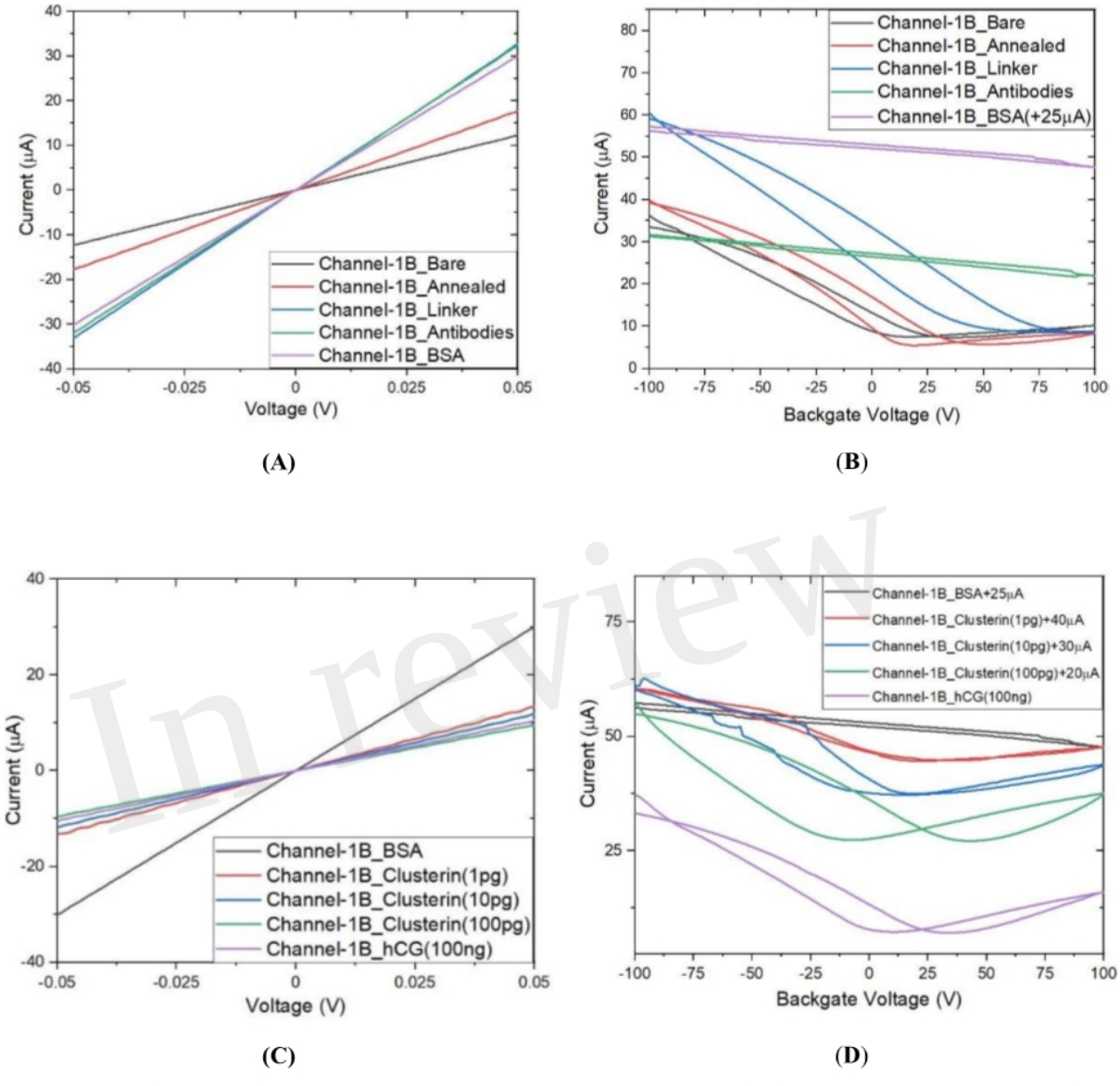

Figure 8. Characteristic curves for Channel-1B **(A)** I_D–V_D output curves for bare to BSA **(B)** I_D–V_G transfer curves for bare to BSA **(C)** I_D–V_D curves for BSA to human chorionic gonadotropin (hCG) (100ng) and **(D)** I_D–V_G curves for BSA to hCG (100ng) with off-set currents shown for clarity. Antigen concentrations are in units of g/mL.

Figure 9:

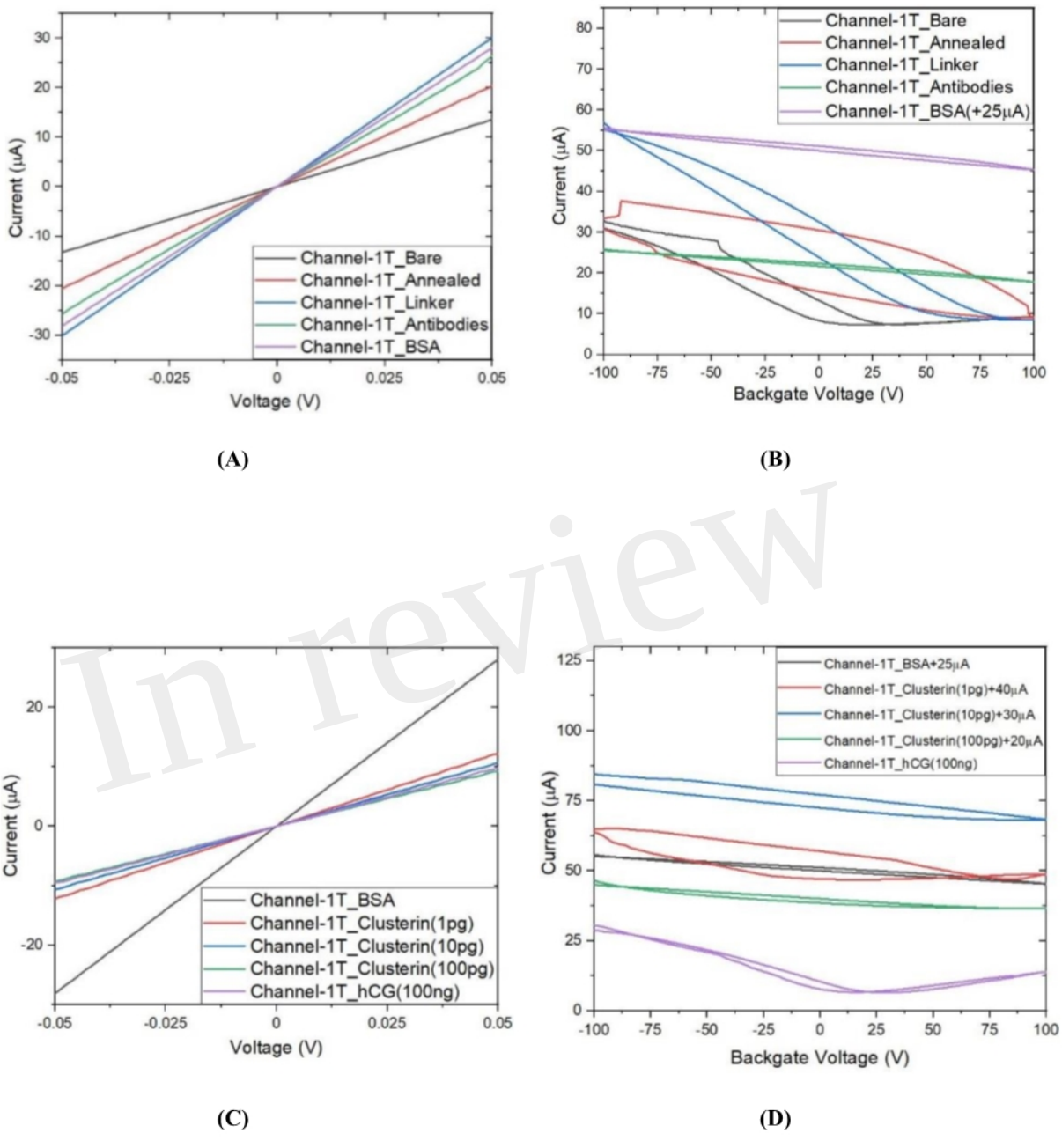

Figure 9. Characteristic curves for Channel-1T **(A)** I_D–V_D output curves for bare to BSA **(B)** I_D–V_G transfer curves for bare to BSA **(C)** I_D–V_D curves for BSA to hCG (100 ng/mL) and **(D)** I_D–V_G curves for BSA to hCG (100 ng/mL), with off-set currents shown for clarity. Antigen concentrations are in units of g/mL.

Figure 10:

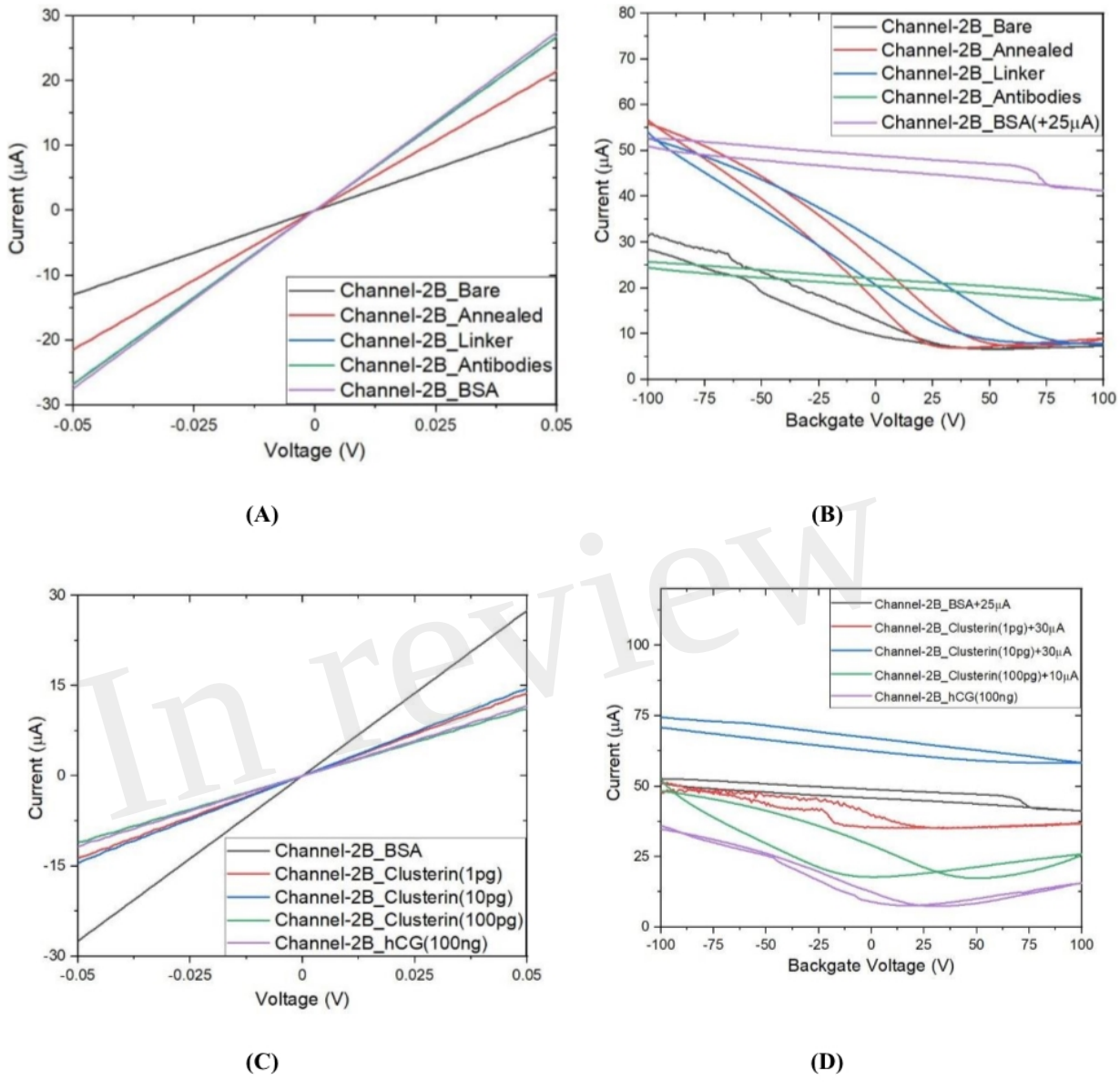

Figure 10. Characteristic curves for Channel-2B **(A)** I_D–V_D output curve for bare to BSA **(B)** I_D–V_G transfer curve for bare to BSA **(C)** I_D–V_D curve for BSA to hCG (100 ng/mL) and **(D)** I_D–V_G curve for BSA to hCG (100 ng/mL), with off-set currents shown for clarity. Antigen concentrations are in units of g/mL.

Figure 11.JPEG

Table 1. The forward and reverse Dirac point voltages (DPV) and the resistance of the three channels. The Dirac point voltages reveal that the GFET is p-doped. Back-gate sweep rate was ~ 20V/s.

Channel	Forward Sweep DCV	Reverse Sweep DCV	Resistance
Channel-1B	17 V	35 V	4086 Ω
Channel-1T	35 V	22 V	3789 Ω
Channel-2B	42 V	51 V	3852 Ω

Table 2. The raw resistance and resistance change (%) for Bare to BSA stages of functionalisation for the three channels and the corresponding mean and standard deviation values. The percentage changes are calculated for the two nearest stages (i.e. Bare to Annealed, Annealed to Linker etc.)

Channel	Bare (Ω)	Annealed (Ω)	ΔR %	Linker (Ω)	ΔR %	Antibodies (Ω)	ΔR %	BSA (Ω)	ΔR %
Channel-1B	4086	2822	−31	1509	−47	1566	+3.8	1660	+6
Channel-1T	3789	2422	−36	1660	−31	1936	+16	1775	−8
Channel-2B	3852	2323	−35	1868	−20	1862	−0.3	1862	−2.4
Mean+/-SD	3909 ± 128	2522 ± 216	−34 ± 2	1679 ± 147	−33 ± 11	1788 ± 160	6.5 ± 7	1766 ± 83	−1 ± 6

Table 3. The raw resistance and resistance change (%) for Clusterin (1pg/mL) to hCG (100ng/mL) stages of functionalisation for the three channels and the corresponding mean and standard deviation values. The Clusterin and hCG concentrations are in units of g/mL.

Channel	Clusterin (1pg)(Ω)	ΔR %	Clusterin (10pg)(Ω)	ΔR %	Clusterin (100pg)(Ω)	ΔR %	hCG (100ng)(Ω)	ΔR%
Channel-1B	3778	+127	4225	+11	5212	+23	4754	−9
Channel-1T	4084	+130	4697	+15	5406	+15	5244	−2
Channel-2B	3657	+101	3429	−6	4524	+32	4257	−6
Mean+/-SD	3840 ± 180	117 ± 13	4117 ± 523	7 ± 9	5047 ± 378	23 ± 7	4752 ± 403	−6 ± 3

Table 4. Other approaches deployed for biosensors in comparison with our four-probe electrical detection technique.

Electrode Materials	Receptor System	Detection Technique	LoD (pg/mL)	Ref.
SPCE-NPAu	SPCE-NPAu/Streptavidin/Biotin-Aβ-42/anti-Aβ/anti-IgG-AP	CV	100	(Rama, González-García et al. 2014)
Gold Nanoparticles	GNP/MUA/NHS-EDC/Aβ(1-42) monoclonal antibody IgG/BSA/Aβ(1-42) peptide solution	EIS	1	(Wu, Ku et al. 2014)
SPCE/Carbon	SPCE/PANHS/Anti-hCG Ab/BSA/hCG	CV/Electrochemical	1	(Damiati, Haslam et al. 2019)
Au Nanoparticles	Au/PSA antibody/BSA/PSA/tPSA	SPR	30	(Uludag and Tothill 2012)
SPCE	SPCE/Pyr-NHS/anti-CLU F(ab')$_2$/BSA/CLU	CV/SWV	1	(Islam, Damiati et al. 2018)
SPR Chip-Gold	Gold film/EDC-NHS/anti-cTnT antibody/BSA/cTnT	SPR	500	(Pawula, Altintas et al. 2016)
Gold nanoparticles	Gold electrode/AuNP/MPA self-assembly/EDC-NHS/BSA/HER2	EIS	500	(Chun, Kim et al. 2013)
Graphite electrodes	Electrode/EDC-NHS/anti-CA125,anti-CA153,anti-CEA/BSA/CA125,CA153,CEA/M-Pt-CA125Ab$_2$,M-Pt-CA153 Ab$_2$,M-Pt-CEA Ab$_2$	DPV	7	(Cui, Wu et al. 2014)
PDMS/AuNP	PDMS/AuNP/anti-human IgG(cTnI)/BSA/human IgG(cTnI)	Colorimetric	10	(Wu, Bian et al. 2010)
GFET	Graphene/Pyr-NHS/anti-CLU/BSA/CLU	4PER	0.21	This work

Figure 11:

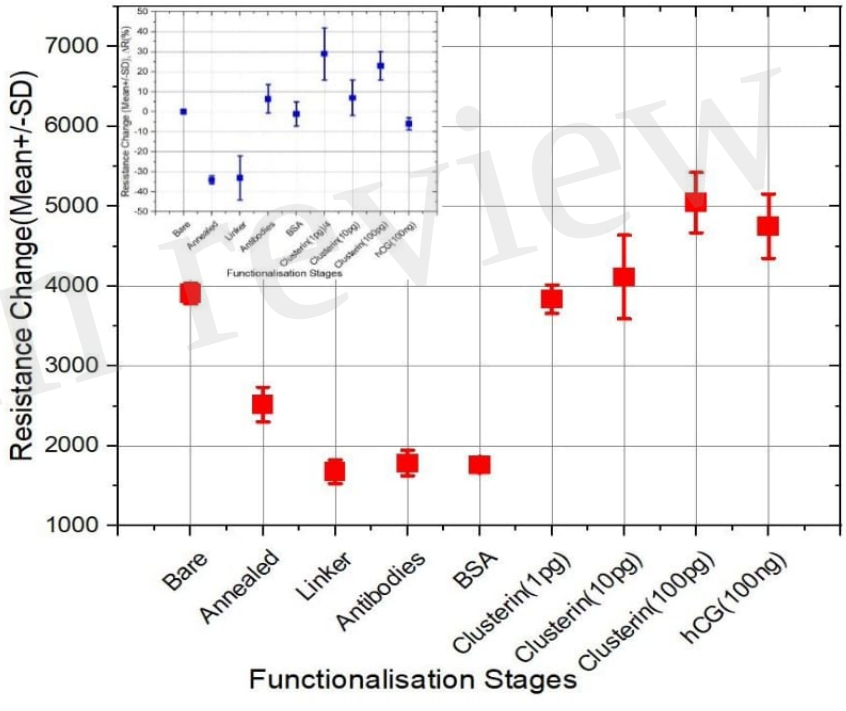

Figure 11. Plots of Resistance change (Mean ±SD) for each functionalization stage with inset showing the corresponding percentage of resistance change relative to the previous stage (with bare stage being 0% by definition) (Mean ±SD). Note, the data in the inset for resistance change at 1pg/mL Clusterin is reduced by a factor of 4 for clarity and Clusterin concentrations are in units of g/mL.